NeuroImage 268 (2023) 119862

Contents lists available at ScienceDirect

NeuroImage

journal homepage: www.elsevier.com/locate/neuroimage

Lead-DBS v3.0: Mapping deep brain stimulation effects to local anatomy and global networks

Clemens Neudorfer[a,b,c,d,*], Konstantin Butenko[c], Simon Oxenford[d], Nanditha Rajamani[d], Johannes Achtzehn[d], Lukas Goede[d,e], Barbara Hollunder[d,f,g], Ana Sofía Ríos[d], Lauren Hart[c], Jordy Tasserie[h], Kavisha B. Fernando[i], T. A. Khoa Nguyen[j,k], Bassam Al-Fatly[d], Matteo Vissani[a,b], Michael Fox[c], R. Mark Richardson[a,b,l], Ursula van Rienen[m,n,o], Andrea A. Kühn[d], Andreas D. Husch[p], Enrico Opri[q], Till Dembek[r], Ningfei Li[d,1,*], Andreas Horn[b,c,d,1,*]

[a] Brain Modulation Lab, Department of Neurosurgery, Massachusetts General Hospital, Boston, MA, 02114, USA
[b] Harvard Medical School, Boston, MA, 02114, USA
[c] Center for Brain Circuit Therapeutics Department of Neurology Brigham & Women's Hospital, Harvard Medical School, Boston, MA, USA
[d] Movement Disorder and Neuromodulation Unit, Department of Neurology, Charité -Universitätsmedizin Berlin, corporate member of Freie Universität Berlin and Humboldt-Universität zu Berlin, Berlin, Germany
[e] Berlin Institute of Health at Charité – Universitätsmedizin Berlin, BIH Biomedical Innovation Academy, BIH Charité Junior Clinician Scientist Program, Berlin, Germany
[f] Einstein Center for Neurosciences Berlin, Charité – Universitätsmedizin Berlin, Berlin, Germany
[g] Berlin School of Mind and Brain, Humboldt-Universität zu Berlin, Berlin, Germany
[h] Division of Neurosurgery, Toronto Western Hospital, University Health Network, University of Toronto, Toronto, ON M5T 2S8, Canada
[i] Melbourne Neuropsychiatry Centre, Department of Psychiatry, The University of Melbourne & Melbourne Health, Melbourne, Australia
[j] Department of Neurosurgery, Inselspital, Bern University Hospital, University of Bern, Bern, Switzerland
[k] ARTORG Center for Biomedical Engineering Research, University of Bern, Bern, Switzerland
[l] Department of Neurosurgery, Massachusetts General Hospital, Harvard Medical School, Boston, United States
[m] Institute of General Electrical Engineering, University of Rostock, Rostock, Germany
[n] Department Life, Light & Matter, University of Rostock, Rostock, Germany
[o] Department Ageing of Individuals and Society, University of Rostock, Rostock, Germany
[p] University of Luxembourg, Luxembourg Centre for Systems Biomedicine, 4362, Esch-sur-Alzette, Luxembourg
[q] Department of Biomedical Engineering, University of Michigan, Ann Arbor, MI, USA
[r] Department of Neurology, Faculty of Medicine and University Hospital Cologne, University of Cologne, Cologne, Germany

ARTICLE INFO

Keywords:
Deep brain stimulation
Imaging
Group-level
Structural connectivity
Functional connectivity

ABSTRACT

Following its introduction in 2014 and with support of a broad international community, the open-source toolbox Lead-DBS has evolved into a comprehensive neuroimaging platform dedicated to localizing, reconstructing, and visualizing electrodes implanted in the human brain, in the context of deep brain stimulation (DBS) and epilepsy monitoring. Expanding clinical indications for DBS, increasing availability of related research tools, and a growing community of clinician-scientist researchers, however, have led to an ongoing need to maintain, update, and standardize the codebase of Lead-DBS. Major development efforts of the platform in recent years have now yielded an end-to-end solution for DBS-based neuroimaging analysis allowing comprehensive image preprocessing, lead localization, stimulation volume modeling, and statistical analysis within a single tool. The aim of the present manuscript is to introduce fundamental additions to the Lead-DBS pipeline including a deformation warpfield editor and novel algorithms for electrode localization. Furthermore, we introduce a total of three comprehensive tools to map DBS effects to local, tract- and brain network-levels. These updates are demonstrated using a single patient example (for subject-level analysis), as well as a retrospective cohort of 51 Parkinson's disease patients who underwent DBS of the subthalamic nucleus (for group-level analysis). Their applicability is

* Corresponding authors.
E-mail addresses: clemens.neudorfer@gmail.com (C. Neudorfer), ningfei.li@charite.de (N. Li), ahorn1@bwh.harvard.edu (A. Horn).
[1] These authors contributed equally

https://doi.org/10.1016/j.neuroimage.2023.119862.
Received 19 July 2022; Received in revised form 22 December 2022; Accepted 3 January 2023
Available online 5 January 2023.
1053-8119/© 2023 Published by Elsevier Inc. This is an open access article under the CC BY-NC-ND license (http://creativecommons.org/licenses/by-nc-nd/4.0/)

further demonstrated by comparing the various methodological choices and the amount of explained variance in clinical outcomes across analysis streams. Finally, based on an increasing need to standardize folder and file naming specifications across research groups in neuroscience, we introduce the brain imaging data structure (BIDS) derivative standard for Lead-DBS. Thus, this multi-institutional collaborative effort represents an important stage in the evolution of a comprehensive, open-source pipeline for DBS imaging and connectomics.

1. Introduction

Over the past three decades deep brain stimulation (DBS) has become a mainstream surgical procedure with the potential to directly probe dysfunctional brain circuits and deliver adjustable stimulation for therapeutic effects in neurological and psychiatric diseases. To investigate the neural substrates underlying therapeutic stimulation, it is integral to establish a direct relationship between the brain areas stimulated by DBS and the resulting clinical response. To do so, precise electrode localizations are necessary, which require the use of dedicated and highly specialized software pipelines. Several platforms – both open source and commercial – have been introduced for electrode localization and reconstruction in recent years (Ahrens et al., 2005; Johansson et al., 2019; Lauro et al., 2016; Miocinovic et al., 2007). The majority of these tools, however, are currently aimed at clinical applications in *individual patients*. Furthermore, knowledge of the methodological details of commercial tools is limited by intellectual property constraints. Finally, numerous tools have lost support or have been discontinued over time. With the introduction of Lead-DBS in 2014, an open-source platform became available to the DBS community offering a semiautomated pipeline for image registration, electrode localization, and stimulation volume modeling (Horn and Kühn, 2015). Following its initial publication, development efforts for the platform continued at multiple institutions providing important methodological updates (Ewert et al., 2018a, 2019a; Hellerbach et al., 2018; Horn et al., 2014, 2019; Horn and Blankenburg, 2016; Husch et al., 2018; Wang et al., 2021). The introduction of the *Lead-Group* toolbox in particular constituted a crucial addition to the platform offering – for the first time – an integrated solution for large-scale analyses of DBS outcomes on a *group level* (Treu et al., 2020). The tool not only allowed comparison of lead localizations across patients and research sites, but also featured rudimentary tools for statistical analysis. Currently, Lead-DBS constitutes the only mature open-source solution that is actively maintained and frequently used in the literature. The repository has received code-contributions by 39 developers from multiple institutions (alongside numerous contributors of data) and consists of Matlab, Python, C and Fortran code components. While the main GUI is currently accessible via Matlab, a compiled standalone version is available, which can be readily used with a GUI or from the command line, without the need for a Matlab installation.

Since the introduction of *Lead-Group*, group-level analysis of DBS outcomes have become a powerful framework to probe the local and network substrates associated with clinical outcomes, behavioral responses, and side-effects during DBS (Horn and Fox, 2020a). Recognizing its potential, a large international community has emerged in recent years developing and applying a vast array of statistical methods to map clinical regressors across DBS applications (Al-Fatly et al., 2019; Dembek et al., 2019; Elias et al., 2020; Horn et al., 2017c; Johnson et al., 2020; Li et al., 2020; Mosley et al., 2020; Neudorfer et al., 2021; Siddiqi et al., 2021). The Lead-DBS toolbox has empowered >500 peer-reviewed papers to date (also see https://www.lead-dbs.org/about/publications/) and has been considered the most comprehensive tool for these analyses by others (Husch et al., 2018; Milchenko et al., 2018). Accuracy of Lead-DBS derived electrode reconstructions was electrophysiologically validated in recent publications from four different groups (Al Awadhi et al., 2022; Nowacki et al., 2018; Oxenford et al., 2021; Rappel et al., 2020). Furthermore, the open-source nature of Lead-DBS and its broad application across continents may foster standardization, or – to paraphrase Latorre et al. – a growing democratization and increased speed of advances in the field (Latorre et al., 2021). With inclusion of novel features into the pipeline, a growing diversity and complexity of employed methods emerges, which bears the risk of jeopardizing the reproducibility of findings. Indeed, it has become increasingly challenging for users to understand the complexities and intricacies of methods included in the Lead-DBS pipeline, which settings to choose and which strategies to follow. For all of the above reasons, we document here the recent methodological advances that have led to Lead-DBS v3.0.

Given the growth and complexity of preprocessing and statistical tools available in Lead-DBS (Fig. 2), it is unfeasible to properly address, document, and evaluate each feature introduced since version 2.0 (Horn et al., 2019) in a single publication as the present one. However, most novel features were already described independently in peer-reviewed work, and key citations are featured within the graphical user interface of the software tool itself. Rather than providing an exhaustive empirical evaluation of each single tool in Lead-DBS, the present manuscript focuses on describing the most salient updates (Fig. 1, bold font). Some of these tools, such as Sweetspot, Fiber Filtering, and Network Mapping Explorer could be considered software with substantial complexity that justify their own methodological papers (e.g. see similar work based on simulated data for sweetspot identification (Dembek et al., 2021a). Here, our aim is to provide an overview of the methods available in Lead-DBS and demonstrate their applicability in single patient- as well as group-level analyses, to provide current and future users with an approachable resource to guide software applications.

2. Methods

2.1. Patient characteristics, imaging, and surgery

In the present manuscript, novel features of Lead-DBS v3.0 were demonstrated either i) in a single example patient, or ii) on a group level, using a previously published cohort of 51 DBS patients. The example patient was an additional 57-year-old male with a 9-year history of Parkinson's disease (PD), who underwent bilateral implantation of segmented DBS leads into the subthalamic nucleus (STN). The patient had a baseline Unified-Parkinson's Disease Rating Scale (UPDRS) III score of 58 (Hoehn and Yahr Scale: 2; Med-OFF), which improved markedly in the ON medication state. Electrode implantation was performed under awake conditions and guided by microelectrode recordings and stimulation testing. In the postoperative course, the patient demonstrated a 55.2% improvement on the UPDRS-III at 12-months follow-up in the Med-OFF state. For group-level analysis we retrospectively evaluated 51 patients (18 females, mean age: 60.0 ± 7.9 years) suffering from treatment-refractory PD. These patients had been well characterized in prior retrospective studies (Horn et al., 2017c, 2017b, 2019; Sobesky et al., 2021a; Treu et al., 2020) and underwent bilateral STN-DBS (model 3389, Medtronic, MN) at Charité – Universitätsmedizin, Berlin between March 2007 and May 2014. Consistent use of this "standard cohort" in the present study had the aim of making results directly comparable to findings previously published in the literature (Horn et al., 2017c, 2019; Sobesky et al., 2021a; Treu et al., 2020). Pre- and postoperative T1-weighted (T1w) and T2-weighted (T2w) magnetic resonance imaging (MRI) scans were obtained using a 1.5 Tesla clinical MRI scanner (NT Intera; Philips Medical Systems, Best, Netherlands). In six of the 51 patients postoperative computed tomography (CT) scans were acquired instead. A detailed overview of employed acquisition parameters can be obtained from the Supplementary Material.

Fig. 1. Overview of the Lead-DBS v3.0 folder structure. Following the release of Lead-DBS v2.0 (gray-blue) in 2019, major changes and updates have been integrated into the Lead-DBS platform (orange). Modifications affected existing preprocessing pipelines for image registration and normalization, but also tools for lead localization, stimulation volume modeling, and statistical analysis. Circles denote the Lead-DBS folder structure with inner circles representing hierarchically higher folders. The size of each segment indicates the number of files contained within each respective subfolder. Color gradients represent the time course of updates to the file and folder structure with greater intensities denoting more recent implementation. Bold fonts denote the most important changes as implemented in Lead-DBS v3.0 which are addressed in the present manuscript.

The surgical techniques associated with STN-DBS have been reported previously (Horn et al., 2017c). In brief, targeting of STN was performed based on T1w and T2w sequences. The preliminary target (reflecting the center of the most distal contact) was identified 12.5 mm lateral, 1.8 mm posterior and 3.5 mm ventral to the midcommissural point (MCP). Intraoperatively, test stimulation and microelectrode recordings were used to guide lead placement and determine the location of optimal symptom improvement. Following electrode implantation, leads were internalized and connected to an internal pulse generator under general anesthesia.

2.2. Volume registrations

2.2.1. Linear (within-patient) co-registration and nonlinear (patient-to-template) normalization

A detailed description of the methods used to perform co-registration and nonlinear normalization in Lead-DBS has been reported previously (Horn et al., 2019; Horn and Kühn, 2015). In brief, following non-parametric, nonuniform, intensity normalization (N4) bias field correction (Tustison et al., 2010) of multimodal preoperative imaging scans, an anchor modality (typically, the preoperative T1w sequence) was identified in each patient and up-sampled to isotropic 0.7 mm resolution. MRI acquisitions were then co-registered to the anchor modality using SPM 12 (https://www.fil.ion.ucl.ac.uk/spm/software/spm12/). Similarly, postoperative CT scans containing the lead location information were co-registered using Advanced Normalization Tools (ANTs; http://stnava.github.io/ANTs/). Results were visually validated to confirm accurate and complete pre-processing.

To evaluate lead placement with respect to neuroanatomical atlases and allow inferences on a group-level (Treu et al., 2020) co-registered patient scans were transformed into ICBM 2009b Nonlinear Asymmetric ('MNI') space applying ANTs Symmetric Normalization (SyN) algorithm (Avants et al., 2011) with the 'effective: low variance + subcortical refinement' preset. This approach has been specifically optimized for non-linear registration of subcortical structures (Ewert et al., 2019a; Vogel et al., 2020) and constitutes the current state-of-the-art in the field (Edlow et al., 2019; Elias et al., 2020; Ewert et al., 2019b; Li et al., 2020). To account for potential pneumocephalus and associated non-linear deformation of brain tissue brain shift correction was applied to postoperative scans (Horn et al., 2019).

2.2.2. Registration refinement using WarpDrive

While the aforementioned registration protocol has been used to create reliable DBS models capable of explaining variance in out-of-sample data (Horn et al., 2017c), automated algorithms may still yield misalignment in the area of interest in some cases. Automated registration of the basal ganglia in particular proves challenging to intensity-based registration methods owing to the lack of image contrast (Neudorfer et al., 2022). This is further emphasized by the need to perform manual performance checks in each patient – even for the best performing algorithms – to ensure consistent registration quality (Ewert et al., 2019a). However, while visual inspection may allow the identification and *exclusion* of subpar registrations, there is a current lack of tools allowing targeted *refinement* of registration in the area of interest.

WarpDrive is a manual refinement toolbox that allows direct manipulation of deformation fields generated during normalization and was specifically created for use within Lead-DBS (Oxenford et al., 2021). The application of WarpDrive constitutes an optional step during normalization and is aimed for use in cases where normalization errors are clearly visible and image quality allows unambiguous refinement. It features a diverse set of tools, which allow identification and correction of registration mismatches based on point-to-point or line-to-line fiducials, as well as a smudge tool to freely add local displacements that are applied with a Gaussian smooth kernel. Following WarpDrive-based refinement, the generated transform is applied to both, electrode and contact positions to accurately map lead locations to MNI space. Conversely, since the generated transform is diffeomorphic, atlas structures may be similarly mapped from MNI space into native space with the same accuracy, hence facilitating precise subcortical segmentations. Here, we demonstrate the applicability of the tool highlighting qualitative differences between automated registration approaches (ANTs SyN, protocol used in Lead-DBS v2) and combined automated and manual approaches (ANTs SyN + WarpDrive). To this end we performed registration of two high-resolution imaging resources, BigBrain (Amunts et al., 2013) and the 7T MRI ex-vivo human brain template (Edlow et al., 2019), investigating registration performance of landmarks crucial to functional neurosurgery, namely STN and anterior commissure. The utility of WarpDrive in a clinical research context was further showcased in the example patient. A quantitative evaluation of WarpDrive will be reported elsewhere.

2.3. Reconstruction of electrode trajectories

2.3.1. Lead localization and determination of lead orientation

Electrode localization was carried out in all patients using the advanced processing pipeline of Lead-DBS v2 (Horn et al., 2019). Specifically, leads were first automatically pre-reconstructed using either the PaCER toolbox (Husch et al., 2018) or the (refined) TRAC/CORE approach (Horn and Kühn, 2015). In cases where these algorithms failed, pre-reconstruction was performed manually using the integrated point-and-click tool or the interface between Lead-DBS and 3D Slicer using the fiducial-based implementation (Fedorov et al., 2012). Electrode localizations were then visualized in the provided user interface and manually refined. Given that the example patient featured directional leads an additional step was required to determine the electrode orientation. Here, version 2.0 of the Directional Orientation Detection (DiODe) algorithm (Dembek et al., 2021b) was adapted for inclusion within Lead-DBS which allows fully-automated and unambiguous detections of lead orientation. Based on a postoperative CT scan this algorithm identifies the slices that feature the strongest electrode artifacts and matches the intensity profile extracted from these artifacts to the expected artifact locations of the DBS lead. Importantly, DiODe v2.0 has only been validated for the Cartesia™ directional lead (Boston Scientific, MA, USA). However, while not phantom-validated, support for the bimodal marker of segmented SenSight™ electrodes by the manufacturer Medtronic have been included as well. Also, based on our experience, the algorithm works well for other manufacturers, e.g., the St. Jude Medical Infinity™ directional leads (Abbott Laboratories, IL, USA), however, imaging constraints would need to be evaluated more carefully for these electrodes owing to the smaller size of their stereotactic markers. For a detailed description and validation of DiODe v2 please refer to (Dembek et al., 2021b).

2.3.2. Estimating the stimulation volume, electric field, and pathway activations

Computational models that estimate the electric field distribution and the extent of stimulated neural tissue are common steps in mapping the local and network effects of DBS on both patient-specific and group level. Recognizing the need for flexible implementation strategies, Lead-DBS v3.0 features different approaches to approximate the electric potential and current distribution of electric fields within neural tissue. In general, excitability metrics have been either based on the electric field (*E-field*) (Åström et al., 2015; Baniasadi et al., 2020; Horn et al., 2019) or computational axon models (Butenko et al., 2020; Butson and McIntyre, 2005; Gunalan et al., 2017; McIntyre et al., 2002). Owing to its computational efficiency and ease of implementation, *E-fields* are broadly used in neuromodulation research and were applied here to investigate both local and network effects of DBS on a group level. Based on these, binary stimulation volumes were additionally calculated in native space using an adaptation of the SimBio/FieldTrip pipeline (Vorwerk et al., 2018) as introduced in Lead-DBS v2 and refined for robustness and precision. Briefly, using the finite element method (FEM),

the static formulation of the Laplace equation was solved in a discretized domain represented by a tetrahedral four-compartment mesh constituting gray matter, white matter, metal, and insulating electrode parts (in native patient space). Following the approach by Åström et al., a heuristic value of 0.2 V/mm was used to threshold E-Field magnitude values into a binary stimulation volume (VTA) (Åström et al., 2015; Horn et al., 2017c; Vasques et al., 2009). In addition, voxel values were represented as (unthresholded) E-field magnitudes in the *E-field* approach. Finally, stimulation volumes were transformed into MNI space using the same refined deformation fields described earlier.

A more elaborate concept to model the biophysical effects of DBS is the one of pathway or tract activation models that take into account underlying white matter anatomy to estimate electric effects of DBS directly on the prevalent tracts (Gunalan et al., 2017; Howell et al., 2019). Instead of quantifying a stimulation volume surrounding the electrodes, this concept places axonal cable models alongside anatomical tracts and estimates whether the electric current imposed by the electrode would induce action potentials. Recently, this concept has entered the open-source domain in form of the OSS-DBS toolbox which facilitates a reproducible, time-efficient, and automated estimation of pathway/tract activation models (Butenko et al., 2020). The development of a bidirectional interface between Lead-DBS and OSS-DBS platforms, as introduced in the present manuscript, extends the capability and functionality of both tools by allowing a seamless transition between platforms. Here, we demonstrate the capabilities of this integrated platform in a cohort of 51 PD patients and further showcase the relationship between stimulation amplitude and extent of activation in a single example case. Details about the applied field and pathway activation modeling are described in (Butenko et al., 2020).

2.4. Connectivity analysis

While Lead-DBS was originally developed to facilitate the localization and reconstruction of DBS electrodes (Horn and Kühn, 2015), significant effort in recent years has been directed towards establishing a reliable and efficient pipeline for group-level neuroimaging analysis. A key development in this process was *Lead Group* (Treu et al., 2020), a toolbox implemented within Lead-DBS which allows visualization of electrodes and calculation of stimulation volumes within and across patient cohorts, as well as rudimentary statistical analyses on a local and network level. As the field of neuroimaging-based DBS research continues to grow, however, novel and increasingly sophisticated methods have been developed to make assumptions about the neuroanatomical and network substrates underlying electrical stimulation. These methods can be generally subdivided into three domains – local mapping approaches, tract level analyses, and network level analyses – each incorporating their own, unique pipelines based on a common denominator, the stimulation volume. To accommodate the richness and diversity of statistical methods that have been introduced within each domain, three distinct toolboxes were implemented in Lead-DBS v3.0, each exhibiting a graphical user interface tailored towards accurate and reproducible analysis of group-level data. First, the *Sweetspot Explorer* has been developed to map local hot- and coldspots to anatomy within and around the DBS target region. Second, the *Fiber Filtering Explorer* can be used to identify tracts associated with observed changes in clinical (or behavioral) outcome. These tracts can be derived from a structural connectome or pathway model. Third, the *Network Mapping Explorer* can be used to associate observed effects with distributed functional or structural brain networks. A classical use-case for all three tools is to map clinical improvement to a local, tract- or network-level. However, virtually any effect (e.g., pre- vs. postoperative changes in behavioral variables or symptoms such as risk-taking/impulsivity, changes in a behavioral task comparing ON vs. OFF stimulation, long-term effects such as cognitive decline) may in principle be mapped using these tools. All toolboxes feature a common workflow in the graphical user interface (or command line) that can be divided into i) *Model Setup*, ii) *Visualization & Thresholding*, and iii) *Crossvalidation & Prediction*:

During *Model Setup* the methods and parameters to generate the computational model are defined. This process incorporates decisions about cohort and subcohort selection, type and extent of stimulation volume, selection of the dependent variable and potential covariates, statistical tests, and – in the case of connectivity analyses – selection of the connectome to be used for seeding. The generated model can be visualized and further adjusted during *Visualization & Thresholding*. Specifically, this step allows thresholding of the generated maps based on a predefined significance level and correction for multiple comparison. For more advanced post-hoc analyses, Lead-DBS v3.0 offers the option to export the generated maps in the NIfTI file format, and additionally as weighted streamlines in the *Fiber Filtering Explorer*. *Crossvalidation & Prediction* constitutes the final step in each of the three tools. This step is crucial in the workflow as it establishes the validity of generated models within and generalizability across cohorts. Validation strategies include permutation-based (Leave-Nothing-Out) approaches, as well as Leave-One-Patient-Out, Leave-One-Cohort-Out, and k-fold (randomized) cross-validations. In addition, it is possible to customize this process and generate predictions for individual patients, as well as predefined (sub-)cohorts and sets. The present study demonstrates the individual frameworks in the context of retrospective analysis of the $n = 51$ patient cohort introduced earlier using Leave-One-Patient-Out and 10-fold cross-validation as measures for model validity.

2.4.1. Sweetspot Explorer

To identify local clusters associated with clinical change Lead-DBS v3.0 has harmonized the fundamental methodological choices of multiple prior publications (Butson et al., 2011; Dembek et al., 2019; Eisenstein et al., 2014; Elias et al., 2020; Horn et al., 2021; Reich et al., 2019) within one single tool. These prior publications used different concepts, such as t-tests vs. Wilcoxon signed rank tests, N-maps, thresholding, and alternate choices of a null model, yielding an extensive parameter space of potential settings. These parameters can be freely adjusted and explored by the user allowing easy implementation of novel concepts, however, to facilitate navigation of methodological choices, the *Sweetspot Explorer* features a "inspired by…" dropdown menu that pre-selects choices as they had been made in aforementioned publications. It is important to note, however, that not all provided presets constitute *exact* reproductions of the analysis pipelines originally used by these groups, but rather reflect the general methodological choices and statistics employed in the different publications. For example, Butson et al. employed a different approach to derive stimulation volumes (Butson et al., 2011), whereas Eisenstein et al. did not rely on calculating binary stimulation volumes, at all (Eisenstein et al., 2014). Similarly, several groups performed additional post-hoc analyses, such as cluster thresholding (Reich et al., 2019) or permutation statistics (Dembek et al., 2019; Eisenstein et al., 2014), which have not been implemented in the tool. A warning dialog notifies the user of these crucial differences and we chose to call the presets "inspired by…" to emphasize that *exact* reproductions of all methods into a single tool are not possible. All but the approach by Horn et al., 2022, are based on binarized stimulation volumes. Hence, patient-specific E-field vector magnitudes were first thresholded at 0.2 V/mm and weighted by their corresponding relative motor improvement from baseline as assessed using UPDRS-III. To this end, each voxel within a patient's stimulation volume was assigned the relative improvement score reported in this patient. These values were then aggregated across patients in a voxel-wise manner and – depending on the employed method – normalized based on stimulation volume (Elias et al., 2020) or amplitude (Dembek et al., 2019). The group mean was then computed by averaging the sum of clinically weighted volumes overlapping a given voxel. In addition to these (binarized) stimulation volume based models, the *Sweetspot Explorer* also incorporates an E-field based approach which has been introduced recently (Horn et al., 2021). This preset calculates the Spearman corre-

lation coefficient between E-field magnitudes and clinical outcome in a voxel-wise manner across cohorts. While some approaches used high thresholds for the raw average improvement maps to control for outlier voxels (Butson et al., 2011) other approaches relied on the generation of *n*-maps. *N*-maps provide voxel-wise insight into the number of stimulation volumes overlapping each voxel and may be thresholded to penalize areas encompassed only by a minority of stimulation volumes and remove outlier voxels. In the present study these *n*-maps were thresholded empirically at 30%. Finally, voxel-wise statistics were performed using one-sample *t*-test (Eisenstein et al., 2014), two-sample *t*-test (Reich et al., 2019), or Wilcoxon-signed rank test (Dembek et al., 2019; Elias et al., 2020) to calculate a *p*-map. This *p*-map was then used to mask the *n*-masked average improvement map. Finally, identified clusters were validated using Leave-One-Patient-Out and 10-fold cross-validation. A complete description of the presets used to compute hotspots within the *Sweetspot Explorer* is outlined in Supplementary Table 1. In-fold predictions can be obtained from Supplementary Table 2.

2.4.2. Fiber Filtering Explorer

Note that the terms 'streamlines' and 'fibers' are used interchangeably in the present manuscript. Code and concepts to identify and isolate streamlines associated with clinical outcome during DBS have been implemented in prior versions of Lead-DBS (Baldermann et al., 2019). However, several methodological advancements have been made subsequently, prompting the development of a proper tool for flexible analyses, the *Fiber Filtering Explorer*. Specifically, the tool incorporates the two key analysis strategies pioneered by our group, as well as a novel integration with OSS-DBS for pathway activation modeling (Butenko et al., 2020). The first strategy relies on a combination of *binary* stimulation volumes and two-sample t-tests to derive streamlines associated with clinical outcome (Baldermann et al., 2019). Here, each individual streamline is iteratively assigned a weight in mass-univariate fashion based on a two-sample *t*-test that compares clinical outcomes between patients' stimulation volumes that either traverse or do not traverse the respective streamline. In other words, for each single streamline, this method divides the investigated cohort into two groups whose underlying stimulation volumes either 'activate' it or not. The second strategy involves a combination of (non-binary) *E-fields* and correlation coefficients (Irmen et al., 2020). Similar to the first strategy, this approach iterates across streamlines in a mass-univariate manner. However, the weight assigned to each streamline is determined by the correlation coefficient calculated between E-field vector magnitudes ('fiber activation') and clinical improvements across patients. The third strategy is comparable to the first and applies the same two-sample *t*-test strategy. However, instead of splitting the cohort based on intersections between tract and patient-specific stimulation volumes, binary tract activations are assessed using the double-cable axon model ((Butenko et al., 2020; Butson and McIntyre, 2005; Gunalan et al., 2017; McIntyre et al., 2002) coupled with the extracellular electric field within OSS-DBS. Streamlines are then weighted by again comparing clinical outcome across activated vs. not activated streamlines. Finally, Lead-DBS also features an option to visualize activated streamlines without conducting statistical tests for both VTA-based and OSS-DBS based approaches. This option can be helpful to visually compare tracts activated e.g., in the top- vs. bottom-responding patients within a cohort.

Using the retrospective patient cohort, the present manuscript demonstrates and compares different methodological approaches comprised within the *Fiber Filtering Explorer*. Specifically, we employed the DBS tractography atlas by Middlebrooks et al. (Middlebrooks et al., 2020) to seed streamlines associated with PD symptom change from VTAs and E-fields, respectively. The three methods described above were then applied.

To identify sensible models of structural connectivity, different combinations of the parameters contained within the *Fiber Filtering Explorer* were iteratively applied across the parameter space using results of a 10-fold cross-validation as an objective function (for a full description of parameters please refer to Supplementary Table 2). For example, for a predefined set of n-thresholds ('Tracts connected to > X% of VTAs') R-values based on 10-fold cross validation were derived by iterating through the full parameter space (i.e., all other parameter choices) while keeping the threshold fixed. This process yielded a distribution of R-values associated with each defined parameter and – when plotted against the remaining set of parameters – would allow assumptions regarding the contribution of a specific parameter to the overall performance of a model. The best performing models (defined based on the highest correlation strength using 10-fold cross-validation) were visualized and compared across analysis streams.

2.4.3. Network Mapping Explorer

While localized hotspots and tracts associated with optimal improvement are meaningful conceptual surrogates to improve DBS targeting and programming, a different question is which whole-brain network should optimally be modulated. Derivation of these estimates involves projections to the cortical surface and calculation of cortico-subcortical connectivity strength by means of voxel-wise correlation. The resulting maps have the potential to inform noninvasive neuromodulation strategies (Fox et al., 2014; Weigand et al., 2018) and lead to a better understanding of diseases and therapeutic strategies (Horn and Fox, 2020a). The DBS network mapping framework was established in 2017 (Horn et al., 2017c) and further developed into a dedicated explorer tool in the latest version of Lead-DBS to facilitate group-level analyses of functional connectivity.

By seeding from calculated stimulation volumes within a functional connectome (derived from resting-state functional MRI (rs-fMRI) data either in the individual patient or in a reference cohort of subjects/patients), estimates of polysynaptic network connectivity across the brain may be derived using the *Network Mapping Explorer*. The tool internally calls *Lead Connectome Mapper* (Horn et al., 2019) and has been updated to accommodate the methodological advancements of recently published work (Ganos et al., 2022; Li et al., 2021; Sobesky et al., 2021a). Furthermore, the *Network Mapping Explorer* allows to effectively generate, explore, and statistically validate network models in a single graphical user interface. Normative functional connectivity maps (fingerprints) seeded from patient-specific stimulation volumes were estimated with the aim of computing an R-map associated with optimal outcome in our retrospective patient cohort. For this purpose, a normative, high-resolution rs-fMRI connectome derived from the Brain Genomics Superstruct Project (Yeo et al., 2011) was used to seed average blood-oxygen level dependent (BOLD) signal fluctuations comprised within patient-specific bilateral stimulation volumes from a total of 1000 healthy subjects. The strength of correlation between the seeded time series and every other voxel outside the stimulation volume was then calculated, averaged across the normative sample, and Fisher z-transformed to derive a normalized connectivity fingerprint for each patient. The resulting fingerprint maps were then correlated with clinical outcome in a voxel-wise manner across the cohort to derive an R-map model associated with optimal connectivity. To this end, several established and robust correlation coefficients were investigated, namely Pearson, Spearman, and Percentage Bend correlation. Model performance was evaluated using Leave-One-Patient-Out and 10-fold cross-validation on unthresholded, p-thresholded (α=0.05), and false discovery rate (FDR) corrected (q<0.05) R-maps. Of note, while not demonstrated here, the *Network Mapping Explorer* also allows analysis of DWI-derived connectivity maps and their correlation with clinical outcome in the context of whole-brain connectivity analysis. This adjustment can be easily made by choosing the respective DWI dataset during connectome selection. However, use cases for structural connectivity analysis with Network Mapping Explorer maximally overlap with the Fiber Filtering Explorer. The former would calculate voxel-wise statistics, the latter tract-wise statistics, which could be statistically advantageous (since the same tract can be modulated in different regions).

2.5. A novel storage format conforming to the brain imaging data structure (BIDS) standard

In the past decade DBS research has evolved radically with studies acquiring rich and complex data ranging from electrode types, stimulation parameters, patient demographics, and outcome measures to multidimensional electrophysiology, imaging, and behavioral datasets. This source data typically serves as the starting point for a multitude of image-processing pipelines that yield highly specific and heterogeneous files and data formats. Although the number of DBS studies using multimodal datasets has drastically increased over the past years there has been no consensus on how to organize and share this data. Currently, DBS data are stored in many different structures, with labs adopting their own methods for data and metadata organization. An extension to the brain imaging data structure (BIDS) standard for iEEG data has been proposed (Holdgraf et al., 2019), but primarily focuses on electrophysiological data. The growth of Lead-DBS and the continuous implementation of methods developed by external contributors and our own group alike has yielded complex folder structures that have been iteratively advanced and extended, albeit at the cost of comprehensibility. This imposes a substantial barrier to data sharing, reproducibility, and efficiency in a highly collaborative field that frequently relies on data exchange across centers to confirm, validate, and generalize findings (Li et al., 2020). Overall, there is a clear need in the community for a standard to better describe DBS imaging data and its experimental context.

In 2016, Gorgolewski et al. introduced BIDS as a standard for organizing and describing neuroscience data and metadata with the aim to make datasets more reproducible, transparent, and reusable (Gorgolewski et al., 2016). BIDS features a standardized specification for folder and file naming, the choice of data formats, and the representation of metadata. Importantly, it is modality-agnostic, offering the opportunity for community-driven extension to new modalities. As a result, BIDS has been successfully extended to fields outside the original specification (written for MRI) including EEG (Pernet et al., 2019), MEG (Nisoet al., 2018), and intracranial EEG (Holdgraf et al., 2019). This paper introduces the extension of the BIDS specification for Lead-DBS with the goal of modularizing single-subject and group-level data imported and generated within Lead-DBS. Specifically, while Lead-DBS has been capable of importing BIDS datasets for a while, the present addition includes storage of a BIDS *derivatives* format of output files created by Lead-DBS, necessitating a much more thorough rewrite of the code-base (295.4k code line additions and 59.4k deletions).

2.6. Methods summary

Fig. 1 features a comprehensive overview of novel tools, that have been implemented in Lead-DBS v3.0. Walkthrough tutorials demonstrating the capabilities of the herein presented modifications, including preprocessing, lead localization, statistical analysis, as well as transition to the BIDS format are available at https://www.lead-dbs.org/helpsupport/knowledge-base/walkthrough-videos/.

3. Results

3.1. Clinical improvement

The cohort of 51 PD patients featured a marked alleviation of parkinsonian symptoms following DBS with a 45.3 ± 23.0% improvement on the UPDRS III motor scale and a consecutive 52.8% reduction in levodopa equivalent daily dosage (LEDD). For a detailed description of patient outcomes please refer to Horn et al. (Horn et al., 2017c, 2019). A similar response in clinical outcome was observed in the 57-year-old example patient who demonstrated a 55.2% UPDRS III improvement 12-months following surgery.

3.2. WarpDrive

While normalization algorithms have advanced in recent years demonstrating accuracies comparable to manual expert segmentation (Ewert et al., 2019b; Vogel et al., 2020) their overall performance may vary across subjects, brain regions, imaging modalities, and template spaces. This is demonstrated in example cases in Fig. 2A-D, where automatic registration of high-resolution templates yielded distinct mismatches at the level of the mesencephalon and the anterior commissure, respectively. Similarly, the low contrast-to-noise ratio within the basal ganglia may impede accurate registration in clinical research settings, resulting in a blurry amalgamation of anatomical structures that lack precision and anatomical detail (Fig. 2E-F). Importantly, poor registration accuracy as a result of poor imaging contrast directly translates into lead localization errors and biased models of DBS response (Neudorfer et al., 2022). WarpDrive allows users to account for the inaccuracies introduced by the normalization algorithm in the region of interest (Fig. 2, right column) reaching expert-level registration accuracy by means of fiducial-based manual refinement of the deformation field (Sharp et al., 2010). While future studies are needed to quantify differences in registration accuracy and determine the amount of variance explained in clinical outcome across normalization strategies, WarpDrive has the potential to pave the way towards clinical applications of registration-dependent methodologies. Specifically, accurate transformation of atlas resources, high-resolution templates, hotspots, and connectivity derived targets into patient-space may be crucial in complementing clinical decision making and informing DBS programming as well as surgical targeting (Oxenford et al., 2021). Furthermore, the adjusted deformation transform allows for a more refined group-level analysis in normalized (e.g., MNI) space. A demo application of WarpDrive demonstrating the refinement of patient-to-atlas fit in a surgical case is provided at https://www.youtube.com/watch?v=VcBXu5BURVI.

3.3. Sweetspot Explorer

To identify areas associated with greatest clinical improvement and determine the neuroanatomical substrates subserving outcome in PD symptom severity we employed and evaluated six different mapping strategies as previously described (Butson et al., 2011; Dembek et al., 2019; Eisenstein et al., 2014; Elias et al., 2020; Horn et al., 2022; Reich et al., 2019). Inspection of these maps revealed clusters within the diencephalon encompassing the motor aspect of STN, extending posteriorly into zona incerta (ZI) and inferiorly into associative STN (Fig. 3). Clusters featured a mean volume of 95.1 ± 19.0 mm^3 (range: 56.4 – 102.9 mm^3). The peak intensities of each respective cluster consistently broadly converged onto the sensorimotor aspect of STN, with approaches by Butson, Elias, Dembek, and Horn each localizing to the dorsoposterolateral aspect of STN (Fig. 3). More dorsal intensity peaks were identified by the Eisenstein method, whereas the approach by Reich yielded peak intensities at the border between sensorimotor and associative STN. The centers of gravity of all investigated approaches formed a distinct cluster within the sensorimotor aspect of STN in close proximity to the center of gravity of the subdivision (average Euclidean distance: 1.61 ± 0.2 mm) and an optimal PD target as meta-analytically defined by Caire et al. (Caire et al., 2013) (converted to MNI space in (Horn et al., 2017a); average Euclidean distance: 1.27 ± 0.22 mm). Validation of robustness by means of Leave-One-Patient-Out and 10-fold cross-validation revealed significant correlations for all investigated approaches with the approaches by Elias et al. and Butson et al. explaining the highest amount of variance in Leave-One-Patient-Out ($R = 0.48$, $p<1.0e-16$) and 10-fold cross-validation ($R = 0.46$, $p<1.0e-16$) designs, respectively. These results, however, were similar and not significantly different to other methods, e.g., the only E-field-based approach (Leave-One-Patient-Out: $R = 0.36$, $p = 0.001$; 10-fold cross-validation: $R = 0.36$, $p = 0.001$). A detailed overview of out-of-sample validations across approaches can be obtained from Fig. 3.

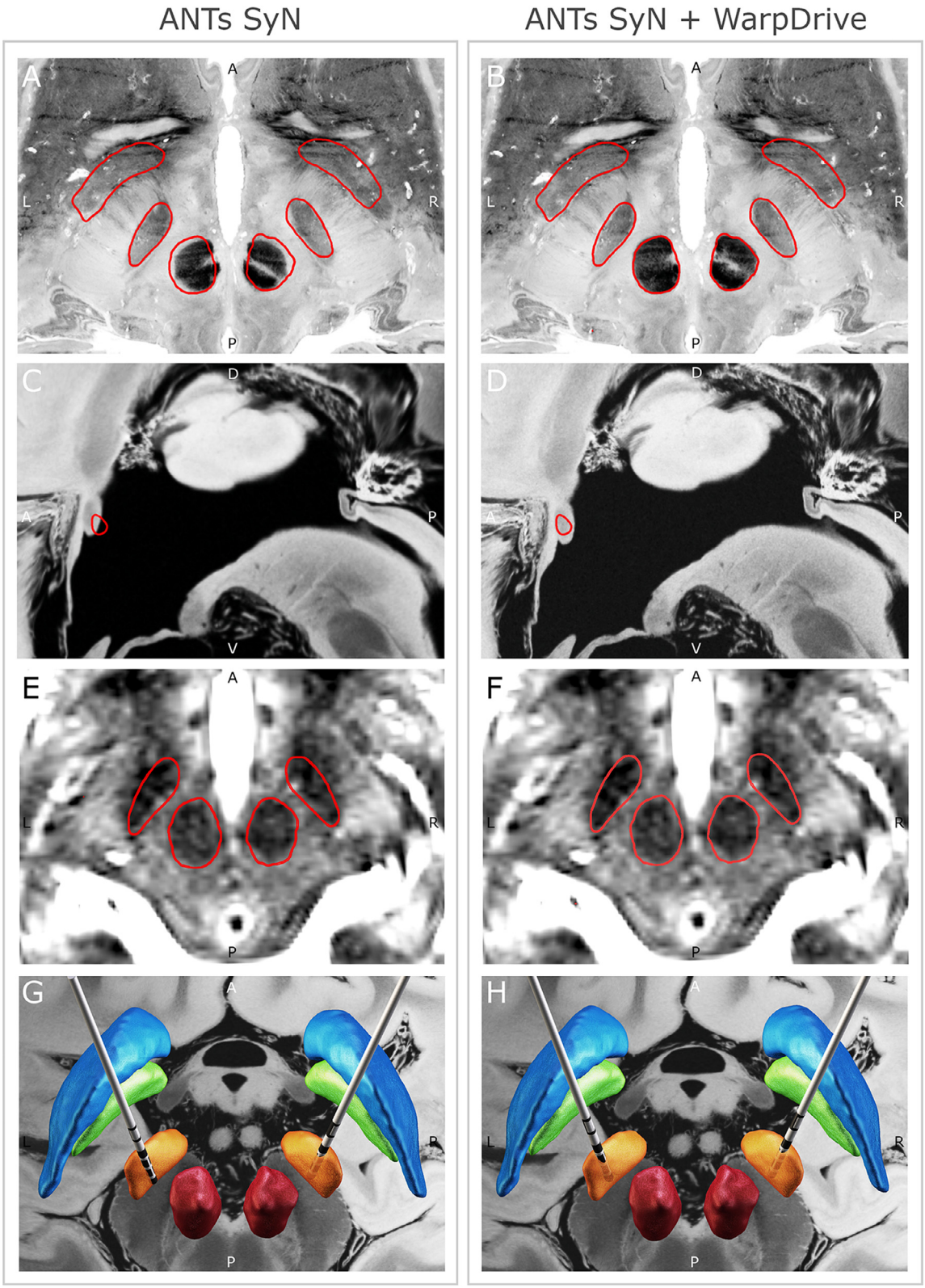

Fig. 2. Comparison of registration accuracy between fully automated non-linear registration (ANTs Syn) and registration employing additional manual refinement using WarpDrive in research and clinical use-case scenarios. (A-D) Research scenario demonstrating high-resolution imaging resources (Amunts et al., 2013; Edlow et al., 2019) featured on coronal (A-B) and sagittal sections (C-D) were transformed into MNI space using a state-of-the art non-linear registration pipeline (ANTs SyN) (left column) and manually refined using WarpDrive (right column). Red outlines feature atlas structures in MNI space (Ewert et al., 2018b; Neudorfer et al., 2020). Note the mismatch between outlines and underlying anatomical structures during automated registration that can be accounted for by means of manual refinement of deformation fields using WarpDrive. (E-H) Clinical research scenario demonstrating the effect of WarpDrive-based refinement on lead localization. (E-F) Atlas structures (red outlines) overlaid on axial T2w MRI scans before (left) and after (right) refinement with WarpDrive. (G-H) 3D representation of reconstructed leads overlaid on the DISTAL atlas in a sample PD patient.

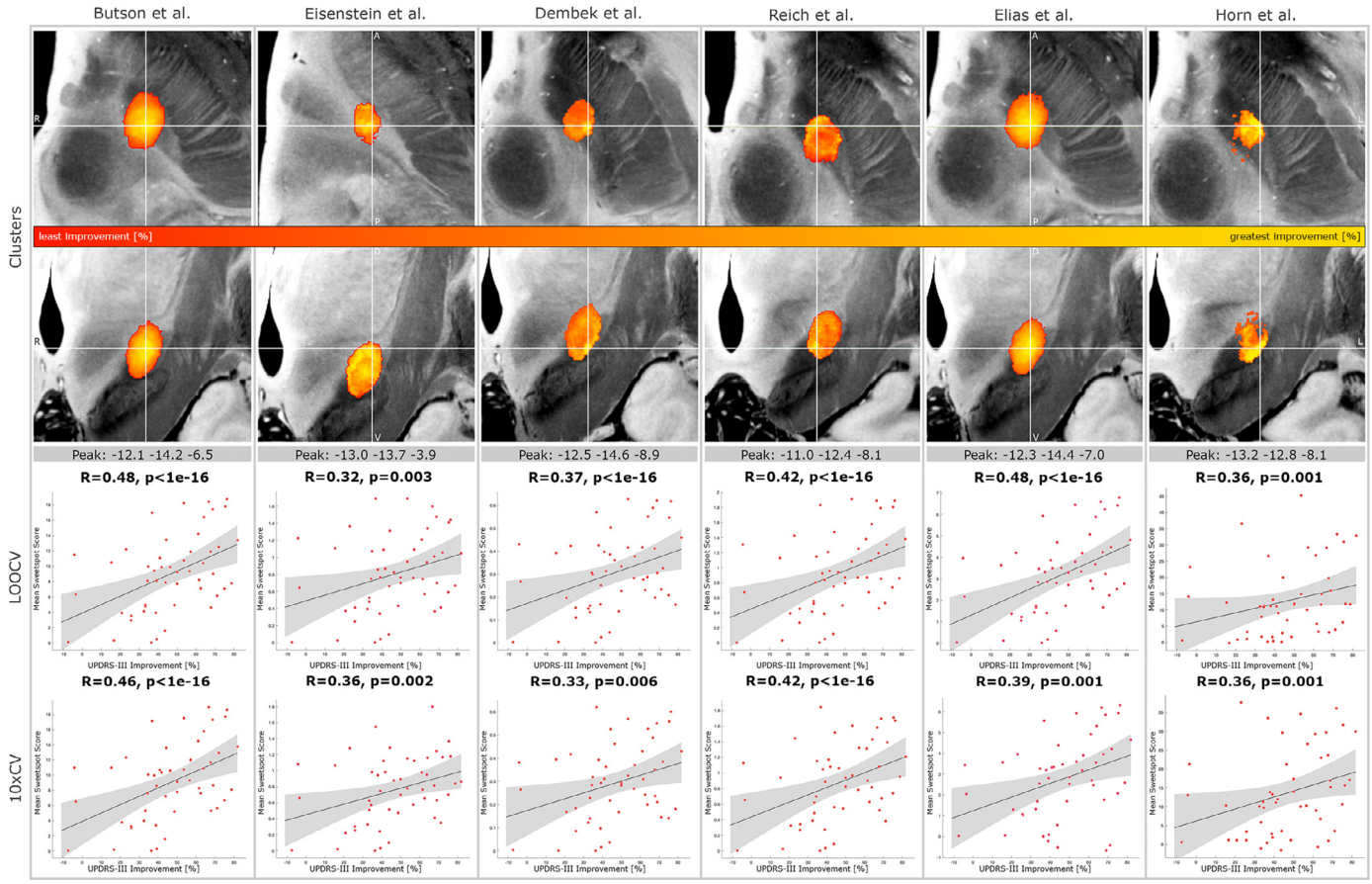

Fig. 3. Hotspot maps of areas associated with clinical improvement in the retrospective patient cohort (n = 51 patients). Stimulation maps were calculated using methodological approaches previously published in the literature (columns) and implemented into the *Sweetspot Explorer*. Note that the presets within this tool do not constitute exact reproductions of the original analysis pipelines but are merely 'inspired' by the methods reported in the published manuscripts. The sweetspot score constitutes the score calculated by overlapping left-out VTA(s) with the sweetspot generated from the remaining stimulation volumes and averaging the sweetspot values (i.e., voxel-wise improvement scores or R-values) encompassed by the left-out VTA(s). Maps are projected on axial (top row) and coronal (second row) slices of a 100 µm resolution 7T brain (Edlow et al., 2019) in Montreal Neurological Institute (MNI) space and aligned at the centers of gravity (crosshairs) of the identified clusters. Color changes denote voxel-wise changes in average clinical outcome and – in the case of the approach by Horn et al. – correlation strengths between E-field magnitude and motor improvement (right column). Peak intensities representing greatest clinical improvement associated with each approach are featured in the center row. Spearman-Correlation coefficients as calculated using Leave-One-Patient-Out (LOOCV) and 10-fold (10xCV) cross-validation are provided in the bottom panels.

3.4. Fiber Filtering Explorer

The *Fiber Filtering Explorer* complements the sweetspot analysis by identifying streamlines associated with changes in clinical outcome. In contrast to the sweetspot analysis, which was informed empirically by previously published approaches (Butson et al., 2011; Dembek et al., 2019; Eisenstein et al., 2014; Elias et al., 2020; Horn et al., 2021; Reich et al., 2019), a data-driven approach was employed to derive suitable preset choices for fiber filtering. Specifically, the parameter space of this methodological framework was probed by iteratively adjusting each tunable parameter without any a-priori assumptions. This approach yielded 2552 models returning predictions, that were validated using 10-fold cross-validation to identify variables that drove model performance and determine the best performing models across analysis streams.

Fig. 4 features the distribution of correlation coefficients associated with 10-fold cross-validation of probed fiber filtering models. By fixing the variables underlying a specific tuning parameter, variables driving model performance could be identified. For example, retention of ≥ 50% of streamlines consistently yielded better performing models across analysis streams. In contrast, transformation of arbitrary streamline value distributions to normal distributions by means of Fisher Z or van Albada transformation yielded less consistent models as compared to no normalization. This was highlighted in particular in the VTA and pathway activation model approaches, where normalization yielded bimodal distributions. The *Fiber Filtering Explorer* allows the omission of streamlines that were only encompassed by a minority of stimulation volumes. Adjustment of this threshold in the range between 10% and 50% yielded overall similar distributions in the E-field and pathway activation model approach suggesting an overall minor effect of n-thresholding on model performance. For the E-field approach, a trend towards improved model performance was observed when using Pearson correlation, followed by Percentage Bend and Spearman correlation.

In a final step, we sought to compare the best performing models derived from each of the three data-driven analysis streams. Identified top performing models were able to explain at least 12% of the observed variance (R = 0.30, p = 0.011) during Leave-one-out cross-validation and at least 20% of the observed variance (R = 0.33, p = 0.008) during 10-fold cross-validation, respectively (Fig. 4, correlation plots). A detailed description of the settings used for model setup, visualization, thresholding, and prediction can be obtained from Supplementary Table 3. Investigation of discriminative tracts revealed overlapping connectivity patterns across models associating streamlines within the hyperdirect pathway with optimal clinical improvements along the motor UPDRS III

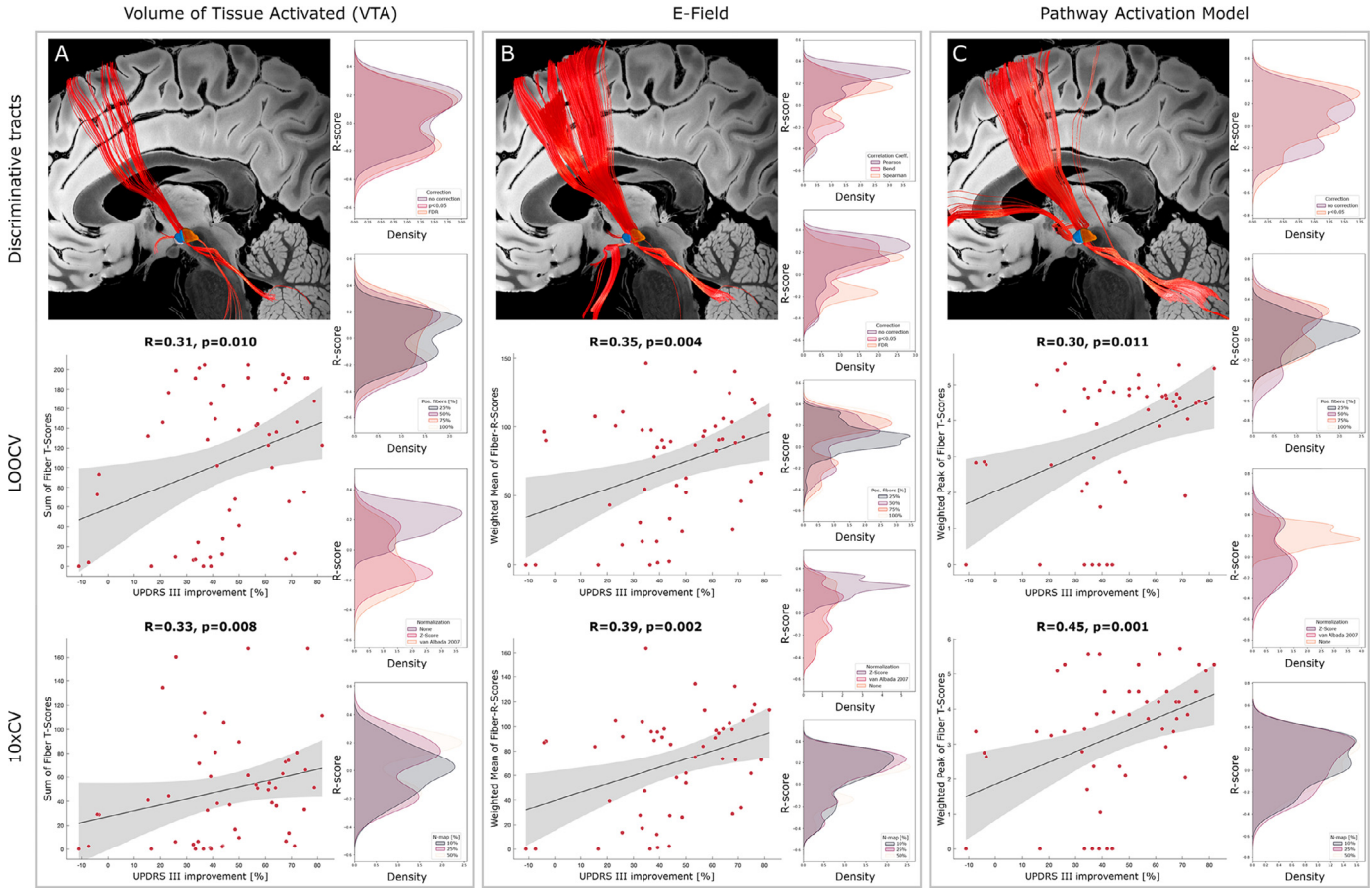

Fig. 4. Model performance probing the parameter space of the Fiber Filtering Explorer. A data-driven approach was employed to derive distributions of model performance using the correlation coefficient derived from 10-fold cross-validation as target. For each analysis stream, the parameter space was probed by iteratively changing the presets contained within the *Fiber Filtering Explorer*; for each analysis stream the distribution of R-values is featured fixing the variables underlying a specific tuning parameter. For each analysis stream (volume of tissue activated vs. E-Field vs pathway activation model) the top performing model was selected and visualized. Note the overall agreement of identified discriminative streamlines despite methodologically different approaches and presets. Correlation plots feature the model performance based on Leave-One-Patient-Out and 10-fold cross-validation. A detailed description of the settings used for model setup, visualization, thresholding, and prediction can be obtained from Supplementary Table 3.

scale. Similarly, models identified the ansa subthalamica as well as cerebellar streamlines that were likely engaged by encroachment of stimulation volumes onto the cerebellothalamic tract within the posterior subthalamic area (PSA). These streamlines were particularly prominent in the pathway activation model (Fig. 4C). Finally, both the E-field approach and the pathway activation model sparsely identified streamlines connecting STN to prefrontal and temporal cortex, suggesting involvement of non-motor regions with optimal clinical outcome.

Taken together, results across fiber filtering analysis streams were overall consistent, revealing comparable models with similar structural connectivity despite employment of different tuning parameters for model generation. Furthermore, we identified a trend of more complex models (OSS-DBS based pathway activation models) yielding slightly more predictive models. Finally, our findings suggest that specific variable presets (see Supplementary Table 3) may be associated with improved and more consistent model performance. These have now been included as default parameter settings within Lead-DBS v3.0.

3.5. Pathway activation modeling in individual patients

As OSS-DBS is optimized for pathway activation modeling, its integration within Lead-DBS generates an efficient workflow for the calculation, visualization, and analysis of fibers activated during DBS. Beyond the aforementioned group-level analysis, this was further demonstrated in an example patient where the dose-response relationship between stimulation amplitude and extent of pathway activation was modeled following electrode localization and reconstruction in Lead-DBS (Fig. 5). Stimulation particularly emphasized the hyperdirect pathway motor fibers, that featured strong activation at low amplitudes that quickly saturated as stimulation currents were increased (Figs. 5A-B). Surrounding tracts demonstrated a sigmoidal activation profile that typically reached its maximum activation at amplitudes > 4 mA (Fig. 5C) emphasizing the increased potential for adverse side effects that are commonly observed under these stimulation conditions (Dayal et al., 2017).

3.6. Network Mapping Explorer

To derive estimates of polysynaptic functional network connectivity across the brain we leveraged the parameter space of the *Network Mapping Explorer* (Fig. 6). A detailed description of the settings used for model setup, visualization, thresholding, and prediction can be obtained from Supplementary Table 5. In-fold predictions for the best performing model based on 10-fold cross-validation are featured in Supplementary Table 6. Of note, the *Network Mapping Explorer* features the overall lowest user degrees of freedom across mapping tools. One reason for this may be that the field of rs-fMRI has already converged on many community standards such as the preprocessing pipelines (Esteban et al., 2019), or the choice of how to calculate functional connectivity from time series (typically Pearson correlation instead of alternative metrics such as mutual information or spectral coherence). Out-of-sample validation

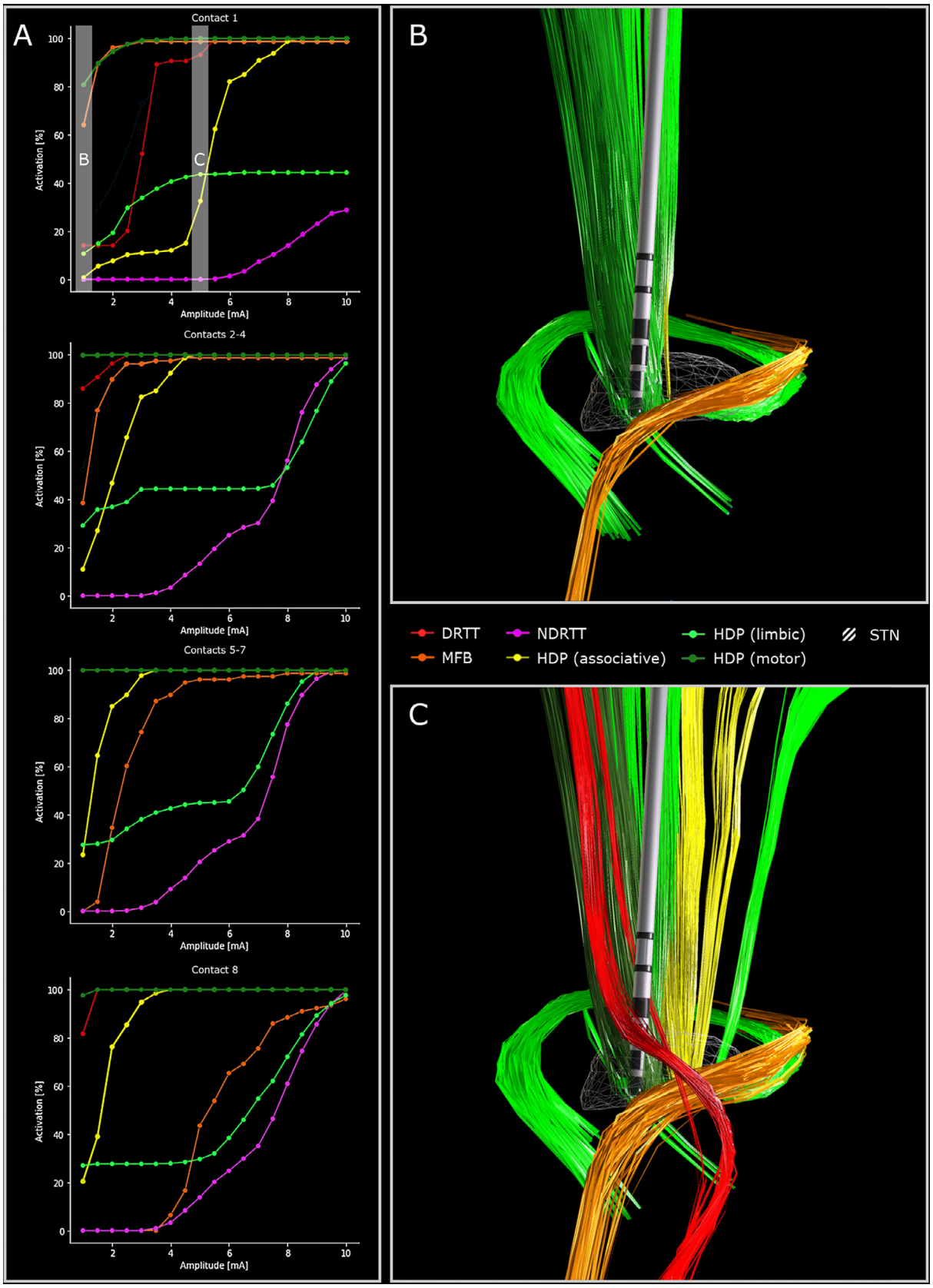

Fig. 5. Pathway activation modeling in an example patient undergoing STN-DBS. (A) Dose-response curves featuring the relationship between stimulation current and extent of pathway activation as modeled using OSS-DBS. Note the sigmoidal activation profiles that quickly saturate in the motor hyperdirect pathway (HDP). (B-C) 3D visualization of pathway activations during stimulation at contact 1 with current amplitudes of 1.0 mA (B) and 5.0 mA (C), respectively. Streamlines were derived from the DBS tractography atlas by Middlebrooks et al. (Middlebrooks et al., 2020).

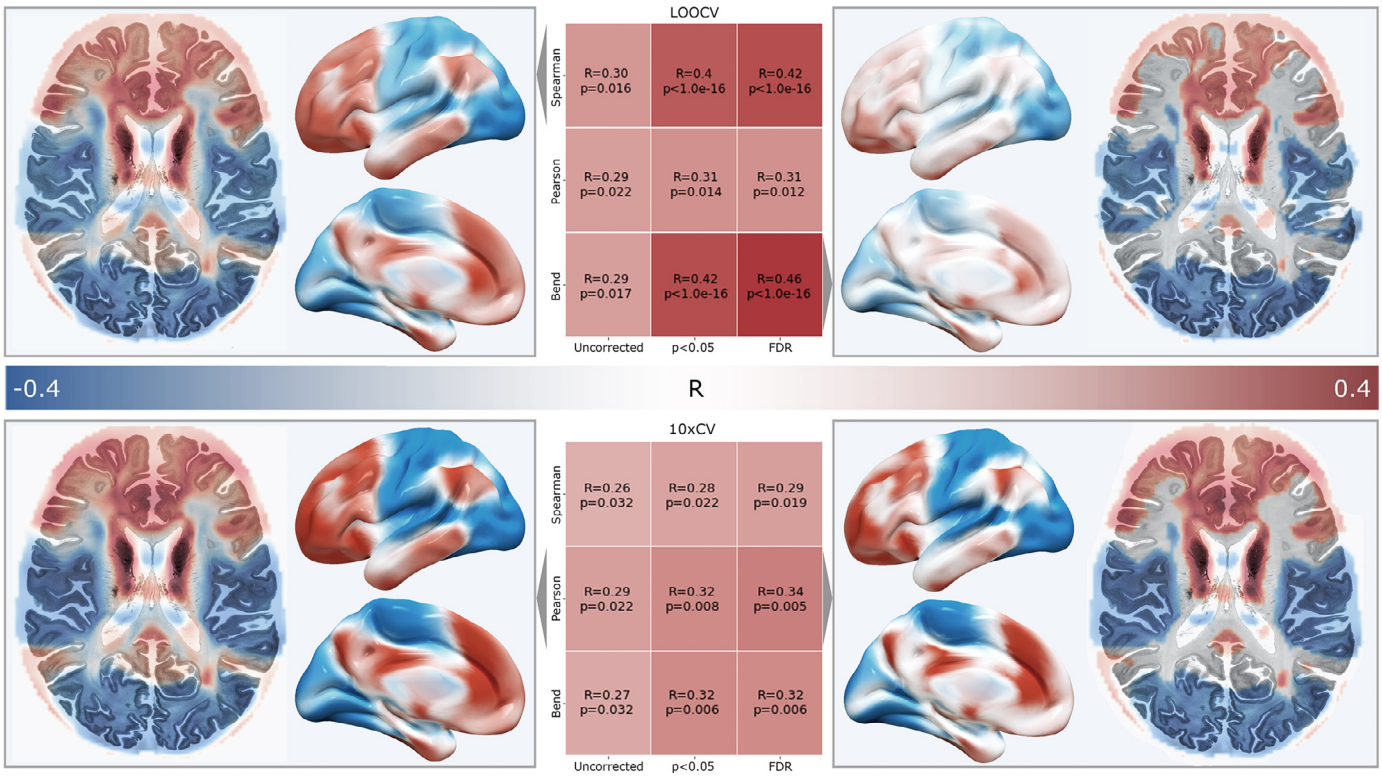

Fig. 6. Investigation of the parameter space underlying the Network Mapping Explorer. R-map models were generated using different correlation coefficients and thresholds (unthresholded, p-thresholded (α=0.05), false discovery rate (FDR) corrected (q<0.05)) and validated using Leave-One-Patient-Out (top row) and 10-fold cross-validation (bottom row) designs. Functional connectivity associated with optimal outcome emphasized premotor (PMA) and supplementary motor area (SMA), anterior cingulate cortex, medial prefrontal cortex (mPFC), thalamus, and cerebellum. The best performing R-map models for uncorrected (left column) and FDR-corrected (right column) models are visualized. Overall, models employing FDR correction yielded the best out-of-sample estimations.

identified significant network predictors of clinical outcome across all investigated models with FDR corrected models yielding the highest predictive power in Leave-One-Patient-Out (R_{Bend}=0.46, p<1.0e-16) and 10-fold cross-validation ($R_{Pearson}$=0.34, p = 0.005) designs.

Identified functional connectivity profiles were consistent across methodologically different approaches featuring activity patterns comparable to previously published literature (Horn et al., 2017c; Sobesky et al., 2021a). Specifically, models identified a positive correlation of clinical outcome with connectivity to premotor (PMA) and supplementary motor area (SMA), anterior cingulate cortex, medial prefrontal cortex (mPFC), thalamus, and cerebellum. In contrast, connectivity to M1 correlated negatively with clinical outcome. In contrast, connectivity to M1 correlated negatively with clinical outcome. The observed anticorrelation may be attributed to reduced positive connectivity to M1, i.e., clinical outcome improved more strongly in patients in which DBS electrode connectivity to M1 was less positive. Alternatively, positive outcome may be associated with stronger negative connectivity. To disambiguate between the two scenarios, we plotted voxel-wise correlations of connectivity to stimulation volumes with clinical improvement (Supplementary Figure 1). Correlation plots revealed that reduced connectivity in M1 was associated with improvement in clinical outcome (Supplementary Figure 1). This has been demonstrated in numerous prior studies (Boutet et al., 2021b; Fox et al., 2014; Horn et al., 2019b, 2017d; Sobesky et al., 2021b).

3.7. Towards integration of the brain imaging data structure (BIDS)

Aiming to standardize folder and file naming conventions and enhance user accessibility, Lead-DBS was modified to (i) read in BIDS formated input data (raw data) and (ii) write out data as a BIDS derivative in a format inspired by existing BIDS standards. Especially the latter part constituted a major effort (800 commits, 770 changed files with 295.4k additions and 59.4k deletions) within our group, which led to a redesigned folder structure including a graphical-user-interface to convert DICOM data into BIDS-conform raw data. Fig. 7 features a comparison between the original data structure implemented in previous versions of Lead-DBS and the updated format conforming to the BIDS standard. Of note, while the raw data folder follows the published BIDS standard, the derivatives folder of Lead-DBS has been adjusted in accordance with the Lead-DBS processing pipeline and passes the BIDS validator. The folder structure follows a logical order incorporating preprocessing, coregistration, normalization, brain shift correction, electrode reconstruction, and stimulation volume modeling steps. Within the Lead-DBS /derivatives folder, image files are stored in the NifTI (.nii) format, whereas metadata are stored either in MATLAB format for tabular data (.mat) or JavaScript Object Notation (JSON) format for 'key:value' pairs (.json). Going forward, we aim to further migrate all .mat files with a low data component to .json format. Support of the compressed NIfTI (.nii.gz) format is currently only implemented in parts of the pipeline since core components heavily build upon reading in headers or single slices / probing NifTI files at specific coordinates. This is not possible in the .gz format without decompressing (and hence reading in) the entire volume, which would lead to extensive speed decrease and I/O load for some of the high-resolution applications that were incorporated within Lead-DBS. While this limitation of the .gz standard does not impede most pipelines, it does so for the precision-imaging case of DBS, where fast and repeated access to uncompressed files is needed in some steps. Finally, log files generated during registration and normalization use the text file format (TXT) extension (.txt). For a detailed overview of how folder and file naming conventions changed and how

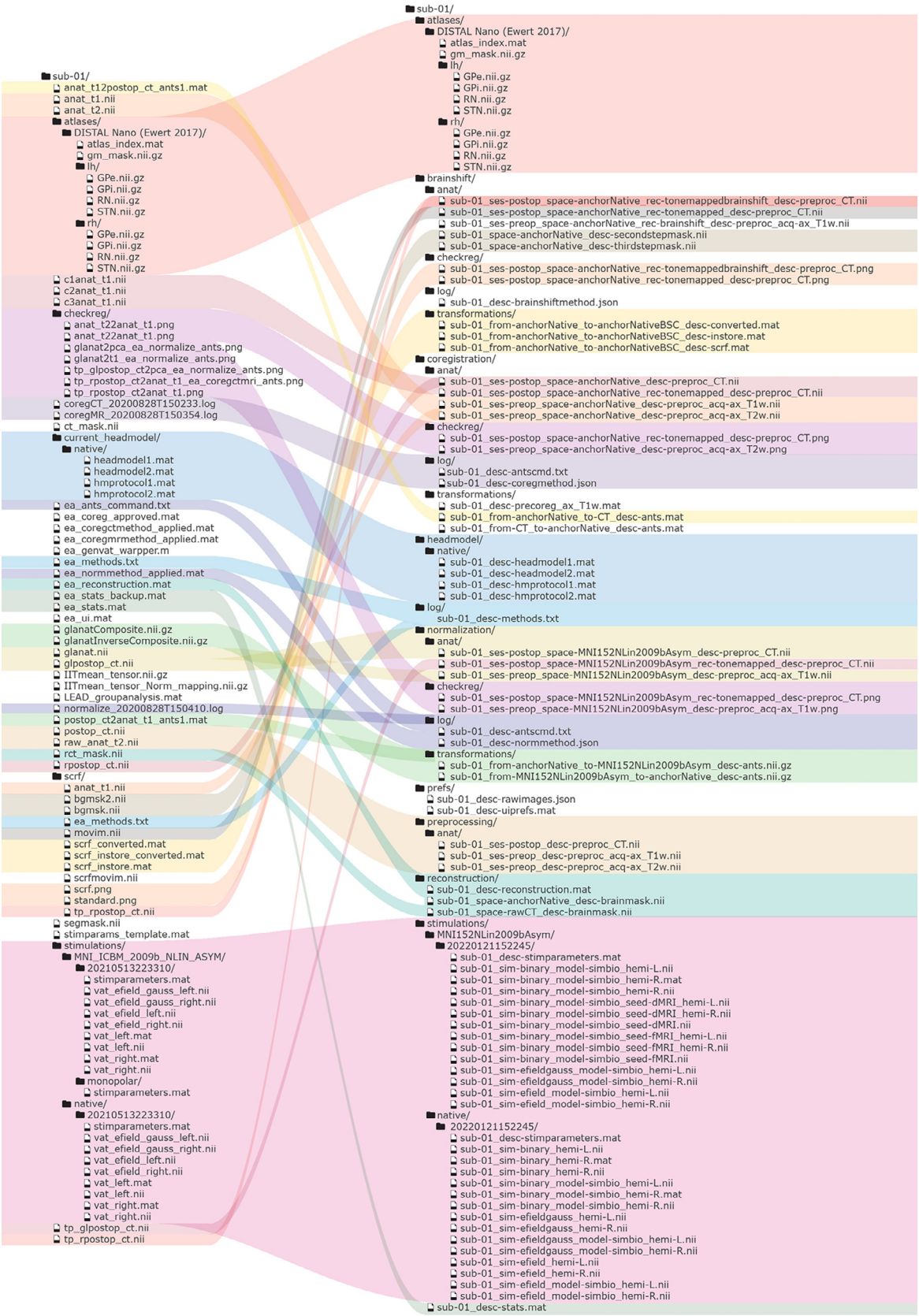

Fig. 7. Adoption of the brain imaging data structure (BIDS) standard into Lead-DBS v3.0. With the introduction of the BIDS standard into Lead-DBS, the conventional folder structure (left column) underwent radical reorganization yielding a modularized layout that features separate folders for each processing step within the Lead-DBS pipeline. In addition, the naming convention for imaging data, tabular data, and metadata was revised. A translation of the original naming convention to the BIDS specification is provided in the figure. For an itemized overview please refer to Supplementary Table 7.

Table 1
Overview of novel neuroimaging resources added to Lead-DBS v3.0 since v2.0. Please refer to https://www.lead-dbs.org/about/data-code-inclusion-philosophy/ for our position on inclusion of external resources into Lead-DBS.

	Name	Description	Reference
Atlases	Subcortical White Matter Pathways	Tractograms describing the main trajectories of thalamocortical, mesocorticolimbic, and cerebellothalamic projections based on surgical interventions in depression, obsessive-compulsive disorder, and essential tremor.	(Avecillas-Chasin et al., 2019)
	Atlas of the Human Hypothalamus	Segmentation of the diencephalon into 13 hypothalamic and 12 extrahypothalamic gray and white matter structures based on a minimum deformation averaging pipeline that produced high-resolution MRI templates for segmentation.	(Neudorfer et al., 2020)
	Hybra PD Atlas	Parcellation map featuring 12 bilateral subcortical structures heavily implicated in Parkinson's disease pathophysiology. The atlas was constructed based on QSM and T1w images in $n = 87$ PD patients.	(Yu et al., 2021)
Connectomes	HCP 1000 normative rs-fMRI connectome	Matrix connectome based on time series of resting state fMRI of 612 healthy subjects from the 1000 HCP cohort.	(Al-Fatly et al. 2022)
	Pediatric Normative Functional Connectome	A resting-state functional connectome generated from scans of 107 neurotypical pediatric-age subjects from the nyu2 sub-cohort of the Consortium for Reliability and Reproducibility.	(Al-Fatly et al. 2022)
Hotspots	Cluster Headache Atlas	DBS effect map associated with symptom relief in 40 patients suffering from cluster headache.	(Nowacki et al., 2020)
	Essential Tremor Hypointensity	The atlas features a (normative) hypointensity marker derived from FGATIR sequences in $n = 46$ subjects that coincides with the optimal DBS target for essential tremor. The probabilistic hot- and coldspots used for validation are provided as well.	(Neudorfer et al., 2022)
	Essential Tremor Probabilistic Mapping Atlas	Hotspot map associated with optimal clinical outcome in essential tremor derived from $n = 119$ DBS patients across five European centers.	(Nowacki et al., 2022)
	Pallidal Dyskinesia Atlas	Sweetspot map featuring regions associated with stimulation-induced dyskinesia during pallidal DBS in $n = 20$ Parkinson's disease patients	(Tsuboi et al., 2021)
	STN Sweetspots	Symptom-specific probabilistic sweetspots obtained from $n = 21$ PD patients who underwent monopolar test stimulation (449 different stimulation settings) following lead implantation.	(Dembek et al., 2019)
	TOR-PSM	Probabilistic maps associated with clinical outcome of DBS across stimulation sites in Parkinson's disease, dystonia, essential tremor, and depression/anorexia nervosa obtained from a total of $n = 482$ patients over a period of 15 years.	(Elias et al., 2020)
	TOR-signPD	Probabilistic maps associated with symptom-specific improvement (bradykinesia, rigidity, tremor, and axial symptoms) in $n = 275$ Parkinson's disease patients.	(Boutet et al., 2021a)
Connectivity maps	Cognitive Decline Network Atlas	Functional whole brain network map associated with cognitive decline during STN-DBS in $n = 44$ patients suffering from therapy-refractory Parkinson's disease.	(Reich et al., 2022)
	Dystonia response tract atlas	Subcortical pathway atlas featuring streamlines associated with optimal treatment response in a total of $n = 80$ patients with generalized and cervical dystonia.	(Horn et al., 2022)
	ET Lesion Network Atlas	Lesion network map derived from $n = 11$ patients with ischemic stroke lesions, who experienced relief of pre-existing essential tremor following stroke.	(Joutsa et al., 2018b)

to translate the original naming convention into the BIDS specification please refer to Fig. 7 and Supplementary Table 7. A walkthrough tutorial demonstrating the migration of Lead-DBS datasets to the BIDS standard is available at https://www.lead-dbs.org/helpsupport/knowledge-base/walkthrough-videos/. Material and tutorials for implementation of the BIDS standard in the broader context of neuroscience can be obtained from https://bids.neuroimaging.io/get_started.html.

Given that the herein presented BIDS derivative has not been reviewed and accepted by the BIDS community as of yet, our addition should be considered a proposal (or derivatives extension) on how to store DBS imaging data. We explicitly welcome developers of similar or accompanying tools to adopt or refine our standard going forward. We argue that adhering to the same storage format could facilitate using multiple different tools on the same dataset and help to further maximize reproducibility and standardization.

3.8. Additional resources

Lead-DBS hosts a large variety of atlases and resources provided by the DBS and neuroimaging community. A general overview of all resources available in Lead-DBS is featured at https://www.lead-dbs.org/helpsupport/knowledge-base/atlasesresources/; table 1 provides a summary of atlases, connectomes, hotspots, and connectivity maps that have been included in Lead-DBS v3.0. Inclusion of datasets into Lead-DBS does not mean endorsement or approval of these external resources by the Lead-DBS development team (https://www.lead-dbs.org/about/data-code-inclusion-philosophy/).

4. Discussion

Based on support by a broad international community, Lead-DBS has evolved into a comprehensive software platform that seamlessly integrates a wide array of neuroimaging tools dedicated to lead localization, reconstruction, and visualization (Horn et al., 2019; Horn and Kühn, 2015). However, as the field of neuroimaging-based DBS, the number of available research tools, and the community continue to grow there is an ongoing need to maintain, update, and standardize the code base of Lead-DBS. These efforts have culminated in the present manuscript which aims to summarize these major changes and amendments to the Lead-DBS pipeline in recent years. With this new release, the largest coding effort in the history of the tool was undertaken and three comprehensive analysis tools as well as two preprocessing tools and an interface to a sister toolbox for electric modeling were developed. Lead-DBS now also adheres to a more systematic input and output file structure within the BIDS framework, which required extensive re-writes of major parts of the software. To demonstrate these modifications, results of various processing steps were visualized in a single patient example and at the group level in a cohort of 51 patients that underwent STN-DBS for treatment-refractory PD. In the former, important changes to the Lead-DBS preprocessing pipeline were demonstrated, namely manual refinement of deformation fields using WarpDrive, unambiguous detection of segmented electrode orientation using DiODe v2, pathway activation modeling, and implementation of the BIDS standard. In the latter, we demonstrated different analysis streams for group-level analysis, their underlying methodological choices, and

their overall convergence onto a consistent profile of optimal outcome across mapping tools. Finally, we showed that the amount of variance explained varies based on the methodological choices.

Consistent with previous reports, analysis streams derived from *Sweetspot, Fiber Filtering*, and *Network Mapping Explorers* identified profiles of clinical improvement within the dorsolateral motor region of STN (Dembek et al., 2019; Elias et al., 2020) connecting to PMA, SMA, ACC, mPFC, and cerebellum, (Boutet et al., 2021b; Horn et al., 2017c; Shen et al., 2020; Sobesky et al., 2021a) and mediating the treatment response by means of hyperdirect pathways from SMA and cerebellothalamic tract modulation (Akram et al., 2017; Gunalan et al., 2017; Nambu et al., 2002; Neumann et al., 2018). Overall these findings are not novel and have been validated previously by independent groups using different modeling approaches (Horn, 2019c; Horn and Fox, 2020b). The established PD circuit model, however, allowed us to leverage a well characterized PD cohort (Horn et al., 2017c, 2019; Sobesky et al., 2021a; Treu et al., 2020) to demonstrate the spectru m of methodological approaches contained within Lead-DBS v3.0.

Previous publications have addressed and compared methodological choices in neuroimaging-based DBS scenarios. For example, Dembek et al. derived local predictors of clinical outcome using *simulated data* (Dembek et al., 2021a). By defining the sensorimotor aspect of STN as the optimal stimulation target, the authors noted marked differences with respect to the spatial distribution of hotspots. Methods employing voxel-wise statistics against average outcomes yielded the best overall performance as evaluated using Dice coefficient and linear regression. In the present study we relied on a well characterized *clinical cohort* to identify local predictors of DBS response. While all investigated models led to significant correlations during cross-validation, differences were observed with respect to the amount of variance explained across models and the location of peak intensities (Fig. 3).

Taken together, our local mapping findings demonstrate the versatility of the *Sweetspot Explorer* in investigating the impact of fundamentally different methodological approaches, but also highlight distinct limitations that need to be addressed in future research. Indeed, in our analysis, we noted stark differences in solutions when applying different methodological concepts. For example, one key issue during sweet spot mapping (when relying on binary VTAs) is that 'rim regions' only receive data from a small number of patients and have the tendency to artifactually drive peak intensities (Dembek et al., 2021a). Given that there is currently no solution to this statistical limitation, we chose to mitigate this issue by employing comparatively high n-thresholds. Overall, this finding illustrates, however, that the optimal method to calculate DBS hotspots has not yet been found or converged upon. Furthermore, it is unclear how well the parameter choices in the present sweetspot analysis generalize to other outcome measures, indications, and DBS targets. This holds especially true given that the Sweetspot Explorer features a vast parameter space that has only been explored in the context of the six previously published presets in the present study ("inspired by" parameter suggestions), not probing the entire parameter space of the tool. Indeed, a proper study exploring exactly why different methods yield different results and which one of them is superior should be undertaken – optimally across multiple datasets, targets, and diseases – in the future. While in prior work, research labs implemented their own code and concepts to map hotspots for research studies, the open-source framework of the Sweetspot Explorer facilitates studies that compare different approaches and could ultimately lead to a gold standard and consensus on how DBS hotspots should be mapped to maximize their validity and reliability.

Structural connectivity analysis was performed using a data-driven approach, which identified the best performing models across three methodologically distinct analysis streams. Investigation of distributions associated with each methodological choice revealed trends with respect to improved model performance when omitting streamlines based on significance and number of stimulation volumes encompassing a streamline. Furthermore, Fisher Z and van Albada transformation yielded less consistent models as compared to no normalization. The reason for this could be that both concepts add a transformation of the results that is different in each cross-validation step. For instance, when the first of the ten folds of patients was left out, the fiber model was created on the remaining nine and the results were z-scored / Gaussianized. In the second fold, the same happened, but this transform was potentially different, adding noise to the final estimates across folds. It is noteworthy that streamlines associated with clinical improvements based on pathway activation models bore similarity to the ones calculated based on simplified models, albeit yielding the overall highest predictive ability (Fig. 4). This finding is in alignment with recent work by Gunalan et al. who identified field cable models to be most accurate for estimating axonal pathway activation as compared to driving force and VTA-based approaches (Gunalan et al., 2018). This finding has relevant implications for future studies seeking to model structural connectivity, since axon activation models come with computational cost and technical demands. Here – depending on the underlying research question – less computationally demanding approaches may serve as an acceptable middle ground to derive estimates of structural connectivity. This could prove especially relevant in clinical settings where access to high performance computers is typically limited, albeit at the cost of a (potentially substantial) decline in predictive accuracy. In contrast, biophysical modeling of DBS associated structural connectivity may provide a more accurate and comprehensive approach to quantify theoretical responses to stimulation at the cellular level (Duffley et al., 2019).

The modeling choices for voxel-wise connectivity estimates as implemented in the *Network Mapping Explorer* are constrained to the choice of correlation coefficient, p-threshold, and method to correct for multiple comparison. Validation of models using Leave-One-Patient-Out and 10-fold cross-validation yielded spatially comparable predictors of outcome, with FDR corrected models demonstrating the overall best performance (Fig. 6). This finding is not surprising, as the removal of false positive voxels likely yields fewer type I errors, hence increasing statistical power.

The mapping tools introduced here offer an extensive range of methodological choices that can be leveraged for model generation, validation, and prediction. This holds especially true for the *Sweetspot* and *Fiber Filtering Explorer* that each offer a larger parameter space that may introduce a risk for bias and confounding. To mitigate this bias for sweetspot mapping, we adopted previously published methodological choices reported by other groups. It is important to note, however, that no unambiguous or conceptual 'ground truth' exists for many of the tunable parameters chosen by these authors. Even if such thresholds existed one could never be certain that the generated models genuinely reflected clinical reality. In consequence, while the methodological choices in the present manuscript may guide future exploration of DBS data, they do not constitute mandatory parameters to be followed rigorously. Since Lead-DBS is a scientific tool, we chose to provide users with the opportunity to instantiate their models in the most sensible fashion to address their scientific questions in use-case scenarios without making a-priori decisions on exactly *how* data should be analyzed. This opens the possibility for flexible and transparent research where models reported in the literature could be reliably reproduced and expanded on. Indeed, the ideal modeling strategy may not rely on fixed and arbitrary thresholds owing to their sensitivity to idiosyncrasies in use-case scenarios. As such, one could envision disease-, target-, and symptom-specific models that are first tuned and cross-validated within training cohorts, confirmed in out-of-sample hold-out test datasets and finally confirmed in prospective fashion within clinical studies.

4.1. Use of Lead-DBS beyond the field of DBS

While the key focus of Lead-DBS is on facilitating DBS imaging research, in many of the tools could be interesting to the broader neuroimaging community. For instance, Lead-DBS unites a multitude of coregistration and normalization algorithms in a single convenient

tool (such as FSL's FLIRT/FNIRT, SPM's Segment, DARTEL & SHOOT and multiple presets for BRAINSfit and ANTs based registrations) as well as WarpDrive, which was introduced here. Taken togehter, these tools make Lead-DBS a versatile "normalization toolbox" that could be useful for most registration problems in the field. The sister application lead connectome is a fully fledged structural and functional connectivity pipeline that is integrated with Lead-DBS, but has been used for other purposes (such as general resting-state, tractography and subsequent modeling analyses as carried out here (Deco et al., 2021; Horn et al., 2019b; Kringelbach et al., 2020)). Finally, the new tools, namely Sweetspot, Fiber Filtering, and Network Mapping Explorer could be modified to map brain lesions associated with specific symptoms, corresponding to a form of voxel-based lesion mapping, disconnectome analysis and functional lesion network mapping analysis. While the Lead Mapper tool has already been used for functional lesion network mapping on multiple occasions (Darby et al., 2017; Ganos et al., 2022; Joutsa et al., 2018a), first reports have applied it for structural lesion network mapping, as well (Bowren et al., 2022; Trapp et al., 2022).

5. Limitations

This present version of Lead-DBS constitutes a major update of the Lead-DBS pipeline, however, despite ongoing development, several limitations persist, which will be described and discussed as follows:

i) Accuracy. In DBS research 'millimeters matter' (Horn et al., 2019) and considerable effort has been invested in the Lead-DBS pipeline to reduce errors associated with image registration, normalization, and lead localization (Dembek et al., 2021b; Horn et al., 2019; Husch et al., 2018). Despite sophisticated tools, however, residual errors may remain, especially in patients featuring changes in brain morphology. Manual refinement tools, such as WarpDrive, may also introduce observer bias and hold the potential of reducing replicability and reproducibility across users and groups. This is further emphasized by the fact that manual refinement of deformation fields requires expert-level understanding of both local anatomy and neuroimaging acquisition/processing. Moving towards potential clinical applications of registration and normalization pipelines (Oxenford et al., 2021) the consideration of residual errors and the quantification thereof remain crucial factors to be addressed.

ii) Stimulation volume modeling. Modeling of DBS E-field distributions is based on multiple assumptions and thresholds, many of which have been defined empirically and remain poorly validated. The findings of the present study indicate that E-field based models perform equally as well as VTA-based models during sweetspot mapping and functional connectivity analysis, while explaining more variance during structural connectivity analysis. Hence, E-field based approaches could be considered a viable alternative to VTA-based approaches. With the introduction of OSS-DBS, sophisticated tools for pathway activation modeling have become openly available that are able to account for some of these limitations, albeit at the cost of computational complexity and cost, as well as necessity of additional prior assumptions. In a research setting, computational cost may have less relevance; in clinical practice, however, there is a need to strike a balance between model tractability and accuracy calling for optimized solutions for stimulation volume modeling in the future.

iii) Statistical methods. Lead-DBS v3.0 introduces three distinct mapping tools, each endowed with a large parameter space. Probing this space currently constitutes a challenge given the need for empirical data, prior assumptions, parameter choices, and thresholds, many of which are poorly validated. In addition, it is currently unclear how well the methodological choices of the Explorer tools generalize to other targets, diseases, and outcome parameters. Hence, it is important to emphasize that Lead-DBS aims to provide useful tools for data analysis without making a-priori decisions on exactly *how* data should be analyzed. Stated bluntly, Lead-DBS should be considered a tool that enables users to carry out scientific analyses, not a tool that carries out these analyses for them. Further research is necessary to evaluate the performance, robustness, and generalizability of demonstrated statistical methods.

iv) Normative connectomes. While the employment of normative connectomes was able to validate clinical outcome in out-of-sample data (Al-Fatly et al., 2019; Germann et al., 2021; Horn et al., 2017c, 2022; Johnson et al., 2020; Li et al., 2020) it is important to note that these datasets lack patient- and pathology-specificity. In contrast to native imaging, however, connectomes offer superior data quality owing to acquisition on specialized hardware, optimized acquisition parameters, and specialized image-processing pipelines (Glasser et al., 2016, 2013; Yeo et al., 2011).

6. Future directions

While Lead-DBS v3.0 has been greatly improved ever since the release of v2.0, further development is planned to address current limitations. During volume registration a major focus will be the optimization and acceleration of registration and normalization routines by means of parallel computing and implementation of neural networks. Recognizing the need for patient-specific analysis, we have further started the implementation of tools to accurately parcellate deep brain structures and reconstruct surfaces in native space using Freesurfer (http://surfer.nmr.mgh.harvard.edu/). Another major focus will be the refinement and expansion of statistical methods available in the introduced Explorer tools. Specifically, we are currently investigating the vast parameter space contained within Sweetspot, Fiber Filtering, and Network Mapping Explorer to identify methodological choices driving model performance. Understanding of these relationships may aide in the optimization of existing tools by e.g., discarding parameter choices that do not contribute to changes in model performance, or refining parameters driving predictions. Finally, novel tools are planned to identify symptom-specific treatment targets with the goal to optimize and tailor stimulation to an individual patient's symptom profile and subjective priorities (Hollunder et al., 2021). As the landscape of neuroimaging and functional neurosurgery continues to evolve and change, further adaptations of the existing pipeline will be required. For example, Lead-DBS currently does not support reconstruction of surface electrodes and electrocorticography (ECoG) arrays. The increased employment of cortical recordings in the field of DBS will, however, requires the implementation of such tools in the future (Gilron et al., 2021; Merk et al., 2021). Future updates will have to address these limitations.

7. Conclusions

In conclusion, we present a thoroughly revised and updated version of the Lead-DBS platform extending its functionality beyond image registration and lead localization to mapping and validation DBS effects to local and network predictors of clinical outcome. Open-source code, version-controlled development, and adherence to widely adopted data standards allow excellent reproducibility necessary to fulfill commonly applied key criteria of good scientific practice. Such transparent research practices constitute crucial steps in validating models prior to translation into clinical practice.

Data and code availability statement

All code used to analyze data presented in the present manuscript is openly available within the Lead-DBS software suite (https://github.com/netstim/leaddbs; https://www.lead-dbs.org/). A detailed description of the settings used for model setup, visualization, thresholding, and prediction for Sweetspot, Fiber Filtering, and Network Mapping Explorer is available in the Supplementary Material of the present

manuscript. Raw data (patient MRI and postoperative CTs) cannot be openly shared because they contain identifiable patient information.

Data Availability

All code is openly available (https://github.com/netstim/leaddbs; https://www.lead-dbs.org/). Raw data cannot be openly shared because they contain identifiable patient information.

Credit authorship contribution statement

Clemens Neudorfer: Conceptualization, Methodology, Investigation, Software, Writing – original draft. **Konstantin Butenko:** Methodology, Software, Investigation, Writing – review & editing. **Simon Oxenford:** Methodology, Software, Writing – review & editing. **Nanditha Rajamani:** Methodology, Software, Writing – review & editing. **Johannes Achtzehn:** Methodology, Software, Writing – review & editing. **Lukas Goede:** Methodology, Software, Writing – review & editing. **Barbara Hollunder:** Methodology, Software, Writing – review & editing. **Ana Sofía Ríos:** Methodology, Software, Writing – review & editing. **Lauren Hart:** Data curation, Methodology, Software, Writing – review & editing. **Jordy Tasserie:** Methodology, Writing – review & editing. **Kavisha B. Fernando:** Methodology, Writing – review & editing. **T. A. Khoa Nguyen:** Methodology, Writing – review & editing. **Bassam Al-Fatly:** Methodology, Writing – review & editing. **Matteo Vissani:** Methodology, Writing – review & editing. **Michael Fox:** Methodology, Writing – review & editing. **R. Mark Richardson:** Writing – review & editing. **Ursula van Rienen:** Writing – review & editing. **Andrea A. Kühn:** Writing – review & editing. **Andreas D. Husch:** Methodology, Software, Writing – review & editing. **Enrico Opri:** Methodology, Software, Writing – review & editing. **Till Dembek:** Methodology, Software, Writing – review & editing. **Ningfei Li:** Conceptualization, Data curation, Methodology, Software, Writing – review & editing, Supervision. **Andreas Horn:** Conceptualization, Data curation, Methodology, Investigation, Software, Writing – original draft, Supervision.

Acknowledgments

The authors would like to thank all the collaborators and contributors to Lead-DBS. A.H. was supported by the German Research Foundation (Deutsche Forschungsgemeinschaft, 424778381 – TRR 295), Deutsches Zentrum für Luft- und Raumfahrt (DynaSti grant within the EU Joint Programme Neurodegenerative Disease Research, JPND), the National Institutes of Health (2R01 MH113929) as well as the New Venture Fund (FFOR Seed Grant). B.H. received support via a scholarship issued by the Einstein Center for Neurosciences Berlin. K.B. was funded by the Deutsche Forschungsgemeinschaft (DFG, German Research Foundation) – SFB 1270/1 – 299150580 and TRR 295 – 424778381. K.B.F. was supported by an Australian Government Research Training Program Scholarship. L.L.G. was supported by the BIH Charité Junior Clinician Scientist Program funded by the Charité – Universitätsmedizin Berlin, and the Berlin Institute of Health at Charité (BIH). MDF was supported by the NIH (R01MH113929, R21MH126271, R56AG069086, R21NS123813) the Ellison / Baszucki Foundation, and the Kaye Family Research Fund). T.A.D. is supported by the Cologne Clinician Scientist Program (CCSP), Faculty of Medicine, University of Cologne and the German Research Foundation (DFG, FI 773/15-1). He also received travel grants and speaker honoraria by Boston Scientific. T.A.K.N. was supported by the Swiss National Science Foundation (186142).

Supplementary materials

Supplementary material associated with this article can be found, in the online version, at doi:10.1016/j.neuroimage.2023.119862.

References

Ahrens, J., Geveci, B., Law, C., 2005. ParaView: an end-user tool for large-data visualization. In: Visualization Handbook. Elsevier, pp. 717–731. doi:10.1016/B978-012387582-2/50038-1.

Akram, H., Georgiev, D., Mahlknecht, P., Hyam, J., Foltynie, T., Limousin, P., Jahanshahi, M., Hariz, M., Zrinzo, L., Ashburner, J., Behrens, T., Sotiropoulos, S.N., Jbabdi, S., De Vita, E., 2017. Subthalamic deep brain stimulation sweet spots and hyperdirect cortical connectivity in Parkinson's disease. Neuroimage 158, 332–345. doi:10.1016/j.neuroimage.2017.07.012.

Al Awadhi, A., Tyrand, R., Horn, A., Kibleur, A., Vincentini, J., Zacharia, A., Burkhard, P.R., Momjian, S., Boëx, C., 2022. Electrophysiological confrontation of Lead-DBS-based electrode localizations in patients with Parkinson's disease undergoing deep brain stimulation. NeuroImage: Clinical 34, 102971. doi:10.1016/j.nicl.2022.102971.

Al-Fatly, B., Ewert, S., Kübler, D., Kroneberg, D., Horn, A., Kühn, A.A., 2019. Connectivity profile of thalamic deep brain stimulation to effectively treat essential tremor. Brain 142, 3086–3098. doi:10.1093/brain/awz236.

Amunts, K., Lepage, C., Borgeat, L., Mohlberg, H., Dickscheid, T., Rousseau, M.-.É., Bludau, S., Bazin, P.-.L., Lewis, L.B., Oros-Peusquens, A.-.M., Shah, N.J., Lippert, T., Zilles, K., Evans, A.C., 2013. BigBrain: an ultrahigh-resolution 3D human brain model. Science 340, 1472–1475. doi:10.1126/science.1235381.

Åström, M., Diczfalusy, E., Martens, H., Wårdell, K., 2015. Relationship between neural activation and electric field distribution during deep brain stimulation. IEEE Trans. Biomed. Eng. 62, 664–672. doi:10.1109/TBME.2014.2363494.

Avants, B.B., Tustison, N.J., Song, G., Cook, P.A., Klein, A., Gee, J.C., 2011. A reproducible evaluation of ANTs similarity metric performance in brain image registration. Neuroimage 54, 2033–2044. doi:10.1016/j.neuroimage.2010.09.025.

Avecillas-Chasin, J.M., Hurwitz, T.A., Bogod, N.M., Honey, C.R., 2019. An analysis of clinical outcome and tractography following bilateral anterior capsulotomy for depression. Stereotact. Funct. Neurosurg. 97, 369–380. doi:10.1159/000505077.

Baldermann, J.C., Melzer, C., Zapf, A., Kohl, S., Timmermann, L., Tittgemeyer, M., Huys, D., Visser-Vandewalle, V., Kühn, A.A., Horn, A., Kuhn, J., 2019. Connectivity profile predictive of effective deep brain stimulation in obsessive-compulsive disorder. Biol. Psychiatry 85, 735–743. doi:10.1016/J.BIOPSYCH.2018.12.019.

Baniasadi, M., Proverbio, D., Gonçalves, J., Hertel, F., Husch, A., 2020. FastField: an open-source toolbox for efficient approximation of deep brain stimulation electric fields. Neuroimage 223, 117330. doi:10.1016/j.neuroimage.2020.117330.

Boutet, A., Germann, J., Gwun, D., Loh, A., Elias, G.J.B., Neudorfer, C., Paff, M., Horn, A., Kuhn, A.A., Munhoz, R.P., Kalia, S.K., Hodaie, M., Kucharczyk, W., Fasano, A., Lozano, A.M., 2021a. Sign-specific stimulation "hot" and "cold" spots in Parkinson's disease validated with machine learning. Brain Commun. 3, fcab027. doi:10.1093/braincomms/fcab027.

Boutet, A., Madhavan, R., Elias, G.J.B., Joel, S.E., Gramer, R., Ranjan, M., Paramanandam, V., Xu, D., Germann, J., Loh, A., Kalia, S.K., Hodaie, M., Li, B., Prasad, S., Coblentz, A., Munhoz, R.P., Ashe, J., Kucharczyk, W., Fasano, A., Lozano, A.M., 2021b. Predicting optimal deep brain stimulation parameters for Parkinson's disease using functional MRI and machine learning. Nat. Commun. 12, 3043. doi:10.1038/s41467-021-23311-9.

Bowren, M., Bruss, J., Manzel, K., Edwards, D., Liu, C., Corbetta, M., Tranel, D., Boes, A.D., 2022. Post-stroke outcomes predicted from multivariate lesion-behaviour and lesion network mapping. Brain 145, 1338–1353. doi:10.1093/brain/awac010.

Butenko, K., Bahls, C., Schröder, M., Köhling, R., van Rienen, U., 2020. OSS-DBS: open-source simulation platform for deep brain stimulation with a comprehensive automated modeling. PLoS Comput. Biol. 16, e1008023. doi:10.1371/journal.pcbi.1008023.

Butson, C.R., Cooper, S.E., Henderson, J.M., Wolgamuth, B., McIntyre, C.C., 2011. Probabilistic analysis of activation volumes generated during deep brain stimulation. Neuroimage 54, 2096–2104. doi:10.1016/j.neuroimage.2010.10.059.

Butson, C.R., McIntyre, C.C., 2005. Tissue and electrode capacitance reduce neural activation volumes during deep brain stimulation. Clin. Neurophysiol. 116, 2490–2500. doi:10.1016/j.clinph.2005.06.023.

Caire, F., Ranoux, D., Guehl, D., Burbaud, P., Cuny, E., 2013. A systematic review of studies on anatomical position of electrode contacts used for chronic subthalamic stimulation in Parkinson's disease. Acta Neurochir. doi:10.1007/s00701-013-1782-1.

Darby, R.R., Horn, A., Cushman, F., Fox, M.D., 2017. Lesion network localization of criminal behavior. Proc Natl Acad Sci USA, 56 –6 doi:10.1073/pnas.1706587115.

Deco, G., Sanz Perl, Y., Vuust, P., Tagliazucchi, E., Kennedy, H., Kringelbach, M.L., 2021. Rare long-range cortical connections enhance human information processing. Curr. Biol. 31, 4436–4448.e5. doi:10.1016/j.cub.2021.07.064.

Dembek, T.A., Baldermann, J.C., Petry-Schmelzer, J., Jergas, H., Treuer, H., Visser-Vandewalle, V., Dafsari, H.S., Barbe, M.T., 2021a. Sweetspot mapping in deep brain stimulation: strengths and limitations of current approaches. Neuromodulation: Technol. Neural Interface 13356. doi:10.1111/ner.13356, ner.

Dembek, T.A., Hellerbach, A., Jergas, H., Eichner, M., Wirths, J., Dafsari, H.S., Barbe, M.T., Hunsche, S., Visser-Vandewalle, V., Treuer, H., 2021b. DiODe v2: unambiguous and fully-automated detection of directional DBS lead orientation. Brain Sci. 11, 1450. doi:10.3390/brainsci11111450.

Dembek, T.A., Roediger, J., Horn, A., Reker, P., Oehrn, C., Dafsari, H.S., Li, N., Kühn, A.A., Fink, G.R., Visser-Vandewalle, V., Barbe, M.T., Timmermann, L., 2019. Probabilistic sweet spots predict motor outcome for deep brain stimulation in Parkinson disease. Ann. Neurol. 86, 527–538. doi:10.1002/ana.25567.

Duffley, G., Anderson, D.N., Vorwerk, J., Dorval, A.D., Butson, C.R., 2019. Evaluation of methodologies for computing the deep brain stimulation volume of tissue activated. J. Neural Eng. 16, 066024. doi:10.1088/1741-2552/ab3c95.

Edlow, B., Mareyam, A., Horn, A., Polimeni, J., Witzel, T., Tisdall, D., Augustinack, J., Stockmann, J., Diamond, B., Stevens, A., Tirrell, L., Folkerth, R., Wald, L., Fischl, B., van der Kouwe, A., 2019. 7 Tesla MRI of the ex vivo human brain at 100 micron resolution. Sci. Data 6. doi:10.1101/649822.

Eisenstein, S.A., Koller, J.M., Black, K.D., Campbell, M.C., Lugar, H.M., Ushe, M., Tabbal, S.D., Karimi, M., Hershey, T., Perlmutter, J.S., Black, K.J., 2014. Functional anatomy of subthalamic nucleus stimulation in Parkinson disease. Ann. Neurol. 76, 279–295. doi:10.1002/ana.24204.

Elias, G.J.B., Boutet, A., Joel, S.E., Germann, J., Gwun, D., Neudorfer, C., Gramer, R.M., Algarni, M., Paramanandam, V., Prasad, S., Beyn, M.E., Horn, A., Madhavan, R., Ranjan, M., Lozano, C.S., Kühn, A.A., Ashe, J., Kucharczyk, W., Munhoz, R.P., Giacobbe, P., Kennedy, S.H., Woodside, D.B., Kalia, S.K., Fasano, A., Hodaie, M., Lozano, A.M., 2020. Probabilistic mapping of deep brain stimulation: insights from 15 years of therapy. Ann. Neurol. doi:10.1002/ana.25975.

Esteban, O., Markiewicz, C.J., Blair, R.W., Moodie, C.A., Isik, A.I., Erramuzpe, A., Kent, J.D., Goncalves, M., DuPre, E., Snyder, M., Oya, H., Ghosh, S.S., Wright, J., Durnez, J., Poldrack, R.A., Gorgolewski, K.J., 2019. fMRIPrep: a robust preprocessing pipeline for functional MRI. Nat. Methods 16, 111–116. doi:10.1038/s41592-018-0235-4.

Ewert, S., Horn, A., Finkel, F., Li, N., Kühn, A.A., Herrington, T.M., 2019a. Optimization and comparative evaluation of nonlinear deformation algorithms for atlas-based segmentation of DBS target nuclei. Neuroimage 184, 586–598. doi:10.1016/j.neuroimage.2018.09.061.

Ewert, S., Horn, A., Finkel, F., Li, N., Kühn, A.A., Herrington, T.M., 2019b. Optimization and comparative evaluation of nonlinear deformation algorithms for atlas-based segmentation of DBS target nuclei. Neuroimage 184, 586–598. doi:10.1016/j.neuroimage.2018.09.061.

Ewert, S., Plettig, P., Li, N., Chakravarty, M.M., Collins, D.L., Herrington, T.M., Kühn, A.A., Horn, A., 2018a. Toward defining deep brain stimulation targets in MNI space: a subcortical atlas based on multimodal MRI, histology and structural connectivity. Neuroimage 170, 271–282. doi:10.1016/j.neuroimage.2017.05.015.

Ewert, S., Plettig, P., Li, N., Chakravarty, M.M., Collins, D.L., Herrington, T.M., Kühn, A.A., Horn, A., 2018b. Toward defining deep brain stimulation targets in MNI space: a subcortical atlas based on multimodal MRI, histology and structural connectivity. Neuroimage 170, 271–282. doi:10.1016/j.neuroimage.2017.05.015.

Fedorov, A., Beichel, R., Kalpathy-Cramer, J., Finet, J., Fillion-Robin, J.-.C., Pujol, S., Bauer, C., Jennings, D., Fennessy, F., Sonka, M., Buatti, J., Aylward, S., Miller, J.V., Pieper, S., Kikinis, R., 2012. 3D slicer as an image computing platform for the Quantitative Imaging Network. Magn. Reson. Imaging 30, 1323–1341. doi:10.1016/j.mri.2012.05.001.

Fox, M.D., Buckner, R.L., Liu, H., Mallar Chakravarty, M., Lozano, A.M., Pascual-Leone, A., 2014. Resting-state networks link invasive and noninvasive brain stimulation across diverse psychiatric and neurological diseases. In: Proceedings of the National Academy of Sciences of the United States of America, 111, pp. E4367–E4375. doi:10.1073/pnas.1405003111.

Ganos, C., Al-Fatly, B., Fischer, J.-.F., Baldermann, J.-.C., Hennen, C., Visser-Vandewalle, V., Neudorfer, C., Martino, D., Li, J., Bouwens, T., Ackermanns, L., Leentjens, A.F.G., Pyatigorskaya, N., Worbe, Y., Fox, M.D., Kühn, A.A., Horn, A., 2022. A neural network for tics: insights from causal brain lesions and deep brain stimulation. Brain awac009. doi:10.1093/brain/awac009.

Germann, J., Elias, G.J.B., Boutet, A., Narang, K., Neudorfer, C., Horn, A., Loh, A., Deeb, W., Salvato, B., Almeida, L., Foote, K.D., Rosenberg, P.B., Tang-Wai, D.F., Wolk, D.A., Burke, A.D., Salloway, S., Sabbagh, M.N., Chakravarty, M.M., Smith, G.S., Lyketsos, C.G., Okun, M.S., Lozano, A.M., 2021. Brain structures and networks responsible for stimulation-induced memory flashbacks during forniceal deep brain stimulation for Alzheimer's disease. Alzheimer's Dementia doi:10.1002/alz.12238, ahead of print.

Gilron, R., Little, S., Perrone, R., Wilt, R., de Hemptinne, C., Yaroshinsky, M.S., Racine, C.A., Wang, S.S., Ostrem, J.L., Larson, P.S., Wang, D.D., Galifianakis, N.B., Bledsoe, I.O., San Luciano, M., Dawes, H.E., Worrell, G.A., Kremen, V., Borton, D.A., Denison, T., Starr, P.A., 2021. Long-term wireless streaming of neural recordings for circuit discovery and adaptive stimulation in individuals with Parkinson's disease. Nat. Biotechnol. 39, 1078–1085. doi:10.1038/s41587-021-00897-5.

Glasser, M.F., Smith, S.M., Marcus, D.S., Andersson, J.L.R., Auerbach, E.J., Behrens, T.E.J., Coalson, T.S., Harms, M.P., Jenkinson, M., Moeller, S., Robinson, E.C., Sotiropoulos, S.N., Xu, J., Yacoub, E., Ugurbil, K., Van Essen, D.C., 2016. The Human Connectome Project's neuroimaging approach. Nat. Neurosci. 19, 1175–1187. doi:10.1038/nn.4361.

Glasser, M.F., Sotiropoulos, S.N., Wilson, J.A., Coalson, T.S., Fischl, B., Andersson, J.L., Xu, J., Jbabdi, S., Webster, M., Polimeni, J.R., Van Essen, D.C., Jenkinson, M., 2013. The minimal preprocessing pipelines for the Human Connectome Project. Neuroimage 80, 105–124. doi:10.1016/j.neuroimage.2013.04.127.

Gorgolewski, K.J., Auer, T., Calhoun, V.D., Craddock, R.C., Das, S., Duff, E.P., Flandin, G., Ghosh, S.S., Glatard, T., Halchenko, Y.O., Handwerker, D.A., Hanke, M., Keator, D., Li, X., Michael, Z., Maumet, C., Nichols, B.N., Nichols, T.E., Pellman, J., Poline, J.-.B., Rokem, A., Schaefer, G., Sochat, V., Triplett, W., Turner, J.A., Varoquaux, G., Poldrack, R.A., 2016. The brain imaging data structure, a format for organizing and describing outputs of neuroimaging experiments. Sci. Data 3, 160044. doi:10.1038/sdata.2016.44.

Gunalan, K., Chaturvedi, A., Howell, B., Duchin, Y., Lempka, S.F., Patriat, R., Sapiro, G., Harel, N., McIntyre, C.C., 2017. Creating and parameterizing patient-specific deep brain stimulation pathway-activation models using the hyperdirect pathway as an example. PLoS One 12, e0176132. doi:10.1371/journal.pone.0176132.

Gunalan, K., Howell, B., McIntyre, C.C., 2018. Quantifying axonal responses in patient-specific models of subthalamic deep brain stimulation. Neuroimage 172, 263–277. doi:10.1016/j.neuroimage.2018.01.015.

Hellerbach, A., Dembek, T.A., Hoevels, M., Holz, J.A., Gierich, A., Luyken, K., Barbe, M.T., Wirths, J., Visser-Vandewalle, V., Treuer, H., 2018. DiODe: directional orientation detection of segmented deep brain stimulation leads: a sequential algorithm based on CT imaging. Stereotact. Funct. Neurosurg. 96, 335–341. doi:10.1159/000494738.

Holdgraf, C., Appelhoff, S., Bickel, S., Bouchard, K., D'Ambrosio, S., David, O., Devinsky, O., Dichter, B., Flinker, A., Foster, B.L., Gorgolewski, K.J., Groen, I., Groppe, D., Gunduz, A., Hamilton, L., Honey, C.J., Jas, M., Knight, R., Lachaux, J.-.P., Lau, J.C., Lee-Messer, C., Lundstrom, B.N., Miller, K.J., Ojemann, J.G., Oostenveld, R., Petridou, N., Piantoni, G., Pigorini, A., Pouratian, N., Ramsey, N.F., Stolk, A., Swann, N.C., Tadel, F., Voytek, B., Wandell, B.A., Winawer, J., Whitaker, K., Zehl, L., Hermes, D., 2019. iEEG-BIDS, extending the Brain Imaging Data Structure specification to human intracranial electrophysiology. Sci. Data 6, 102. doi:10.1038/s41597-019-0105-7.

Horn, A., 2019c. The impact of modern-day neuroimaging on the field of deep brain stimulation. Curr. Opin. Neurol. 32, 511–520. doi:10.1097/WCO.0000000000000679.

Horn, A., Blankenburg, F., 2016. Toward a standardized structural-functional group connectome in MNI space. Neuroimage 124, 310–322. doi:10.1016/j.neuroimage.2015.08.048.

Horn, A., Fox, M.D., 2020a. Opportunities of connectomic neuromodulation. Neuroimage 221, 117180. doi:10.1016/j.neuroimage.2020.117180.

Horn, A., Kühn, A.A., 2015. Lead-DBS: a toolbox for deep brain stimulation electrode localizations and visualizations. Neuroimage 107, 127–135. doi:10.1016/j.neuroimage.2014.12.002.

Horn, A., Kühn, A.A., Merkl, A., Shih, L., Alterman, R., Fox, M., 2017a. Probabilistic conversion of neurosurgical DBS electrode coordinates into MNI space. Neuroimage 150, 395–404. doi:10.1016/j.neuroimage.2017.02.004.

Horn, A., Li, N., Dembek, T.A., Kappel, A., Boulay, C., Ewert, S., Tietze, A., Husch, A., Perera, T., Neumann, W.-.J., Reisert, M., Si, H., Oostenveld, R., Rorden, C., Yeh, F.-.C., Fang, Q., Herrington, T.M., Vorwerk, J., Kühn, A.A., 2019. Lead-DBS v2: towards a comprehensive pipeline for deep brain stimulation imaging. Neuroimage 184, 293–316. doi:10.1016/j.neuroimage.2018.08.068.

Horn, A., Neumann, W.J., Degen, K., Schneider, G.H., Kühn, A.A., 2017b. Toward an electrophysiological "Sweet spot" for deep brain stimulation in the subthalamic nucleus. Hum. Brain Mapp. 38, 3377–3390. doi:10.1002/hbm.23594.

Horn, A., Ostwald, D., Reisert, M., Blankenburg, F., 2014. The structural–functional connectome and the default mode network of the human brain. Neuroimage 102, 142–151. doi:10.1016/j.neuroimage.2013.09.069.

Horn, A., Reich, M., Ewert, S., Li, N., Al-Fatly, B., Lange, F., Roothans, J., Oxenford, S., Horn, I., Paschen, S., Runge, J., Wodarg, F., Witt, K., Nickl, R.C., Wittstock, M., Schneider, G.-.H., Mahlknecht, P., Poewe, W., Eisner, W., Helmers, A.-.K., Matthies, C., Krauss, J.K., Deuschl, G., Volkmann, J., Kühn, A., 2021. Differential Deep Brain Stimulation Sites and Networks for Cervical vs. Generalized Dystonia. medRxiv 2021.07.28.21261289 doi:10.1101/2021.07.28.21261289.

Horn, A., Reich, M., Vorwerk, J., Li, N., Wenzel, G., Fang, Q., Schmitz-Hübsch, T., Nickl, R., Kupsch, A., Volkmann, J., Kühn, A.A., Fox, M.D., 2017c. Connectivity Predicts deep brain stimulation outcome in Parkinson disease. Ann. Neurol. 82, 67–78. doi:10.1002/ana.24974.

Horn, A., Reich, M.M., Ewert, S., Li, N., Al-Fatly, B., Lange, F., Roothans, J., Oxenford, S., Horn, I., Paschen, S., Runge, J., Wodarg, F., Witt, K., Nickl, R.C., Wittstock, M., Schneider, G.-.H., Mahlknecht, P., Poewe, W., Eisner, W., Helmers, A.-.K., Matthies, C., Krauss, J.K., Deuschl, G., Volkmann, J., Kühn, A.A., 2022. Optimal deep brain stimulation sites and networks for cervical vs. generalized dystonia. In: Proceedings of the National Academy of Sciences, 119 doi:10.1073/pnas.2114985119.

Horn, A., Wenzel, G., Irmen, F., Huebl, J., Li, N., Neumann, W.-.J., Krause, P., Bohner, G., Scheel, M., Kühn, A.A., 2019b. Deep brain stimulation induced normalization of the human functional connectome in Parkinson's disease. Brain 18, 130. doi:10.1093/brain/awz239, –15.

Howell, B., Choi, K.S., Gunalan, K., Rajendra, J., Mayberg, H.S., McIntyre, C.C., 2019. Quantifying the axonal pathways directly stimulated in therapeutic subcallosal cingulate deep brain stimulation. Hum. Brain Mapp. 40, 889–903. doi:10.1002/hbm.24419.

Husch, A., Petersen, V., M, Gemmar, P., Goncalves, J., Hertel, F., 2018. PaCER - a fully automated method for electrode trajectory and contact reconstruction in deep brain stimulation. NeuroImage: Clinical 17, 80–89. doi:10.1016/j.nicl.2017.10.004.

Irmen, F., Horn, A., Mosley, P., Perry, A., Petry-Schmelzer, J.N., Dafsari, H.S., Barbe, M., Visser-Vandewalle, V., Schneider, G.H., Li, N., Kübler, D., Wenzel, G., Kühn, A.A., 2020. Left prefrontal connectivity links subthalamic stimulation with depressive symptoms. Ann. Neurol. 87, 962–975. doi:10.1002/ana.25734.

Johansson, J.D., Alonso, F., Wardell, K., 2019. Patient-specific simulations of deep brain stimulation electric field with aid of in-house software ELMA. In: 2019 41st Annual International Conference of the IEEE Engineering in Medicine and Biology Society (EMBC). IEEE, pp. 5212–5216. doi:10.1109/EMBC.2019.8856307.

Johnson, K.A., Duffley, G., Anderson, D.N., Ostrem, J.L., Welter, M.-.L., Baldermann, J.C., Kuhn, J., Huys, D., Visser-Vandewalle, V., Foltynie, T., Zrinzo, L., Hariz, M., Leentjens, A.F.G., Mogilner, A.Y., Pourfar, M.H., Almeida, L., Gunduz, A., Foote, K.D., Okun, M.S., Butson, C.R., 2020. Structural connectivity predicts clinical outcomes of deep brain stimulation for Tourette syndrome. Brain 143, 2607–2623. doi:10.1093/brain/awaa188.

Joutsa, J., Horn, A., Hsu, J., Fox, M.D., 2018a. Localizing parkinsonism based on focal brain lesions. Brain 141, 2445–2456. doi:10.1093/brain/awy161.

Joutsa, J., Shih, L.C., Horn, A., Reich, M.M., Wu, O., Rost, N.S., Fox, M.D., 2018b. Identifying therapeutic targets from spontaneous beneficial brain lesions. Ann. Neurol. 84, 153–157. doi:10.1002/ana.25285.

Kringelbach, M.L., Cruzat, J., Cabral, J., Knudsen, G.M., Carhart-Harris, R., Whybrow, P.C., Logothetis, N.K., Deco, G., 2020. Dynamic coupling of whole-brain neuronal and neurotransmitter systems. In: Proc. Natl. Acad. Sci. U.S.A., 117, pp. 9566–9576. doi:10.1073/pnas.1921475117.

Latorre, A., Rocchi, L., Sadnicka, A., 2021. The expanding horizon of neural stimulation for hyperkinetic movement disorders. Front. Neurol. 12. doi:10.3389/fneur.2021.669690.

Lauro, P.M., Vanegas-Arroyave, N., Huang, L., Taylor, P.A., Zaghloul, K.A., Lungu, C., Saad, Z.S., Horovitz, S.G., 2016. DBSproc: an open source process for DBS electrode localization and tractographic analysis. Hum. Brain Mapp. 37, 422–433. doi:10.1002/hbm.23039.

Li, N., Baldermann, J.C., Kibleur, A., Treu, S., Akram, H., Elias, G.J.B., Boutet, A., Lozano, A.M., Al-Fatly, B., Strange, B., Barcia, J.A., Zrinzo, L., Joyce, E., Chabardes, S., Visser-Vandewalle, V., Polosan, M., Kuhn, J., Kühn, A.A., Horn, A., 2020. A unified connectomic target for deep brain stimulation in obsessive-compulsive disorder. Nat. Commun. 11, 3364. doi:10.1038/s41467-020-16734-3.

Li, N., Hollunder, B., Baldermann, J.C., Kibleur, A., Treu, S., Akram, H., Al-Fatly, B., Strange, B.A., Barcia, J.A., Zrinzo, L., Joyce, E.M., Chabardes, S., Visser-Vandewalle, V., Polosan, M., Kuhn, J., Kühn, A.A., Horn, A., 2021. A unified functional network target for deep brain stimulation in obsessive-compulsive disorder. Biol. Psychiatry 90, 701–713. doi:10.1016/j.biopsych.2021.04.006.

McIntyre, C.C., Richardson, A.G., Grill, W.M., 2002. Modeling the excitability of mammalian nerve fibers: influence of afterpotentials on the recovery cycle. J. Neurophysiol. 87, 995–1006. doi:10.1152/jn.00353.2001.

Merk, T., Peterson, V., Lipski, W., Blankertz, B., Turner, R.S., Li, N., Horn, A., Kühn, A.A., Richardson, R.M., Neumann, W.-.J., 2021. Electrocorticography is Superior to Subthalamic Local Field Potentials for Movement Decoding in Parkinson's Disease. bioRxiv 2021.04.24.441207. doi:10.1101/2021.04.24.441207.

Middlebrooks, E.H., Domingo, R.A., Vivas-Buitrago, T., Okromelidze, L., Tsuboi, T., Wong, J.K., Eisinger, R.S., Almeida, L., Burns, M.R., Horn, A., Uitti, R.J., Wharen, R.E., Holanda, V.M., Grewal, S.S., 2020. Neuroimaging advances in deep brain stimulation: review of indications, anatomy, and brain connectomics. Am. J. Neuroradiol. 41, 1558–1568. doi:10.3174/ajnr.A6693.

Milchenko, M., Snyder, A.Z., Campbell, M.C., Dowling, J.L., Rich, K.M., Brier, L.M., Perlmutter, J.S., Norris, S.A., 2018. ESM-CT: a precise method for localization of DBS electrodes in CT images. J. Neurosci. Methods 308, 366–376. doi:10.1016/j.jneumeth.2018.09.009.

Miocinovic, S., Noecker, A.M., Maks, C.B., Butson, C.R., McIntyre, C.C., 2007. Cicerone: stereotactic neurophysiological recording and deep brain stimulation electrode placement software system. In: Acta Neurochirurgica. Springer Vienna, Vienna, pp. 561–567. doi:10.1007/978-3-211-33081-4_65.

Mosley, P.E., Paliwal, S., Robinson, K., Coyne, T., Silburn, P., Tittgemeyer, M., Stephan, K.E., Perry, A., Breakspear, M., 2020. The structural connectivity of subthalamic deep brain stimulation correlates with impulsivity in Parkinson's disease. Brain 143, 2235–2254. doi:10.1093/brain/awaa148.

Nambu, A., Tokuno, H., Takada, M., 2002. Functional significance of the cortico-subthalamo-pallidal "hyperdirect" pathway. Neurosci. Res. 43, 111–117.

Neudorfer, C., Elias, G.J.B., Jakobs, M., Boutet, A., Germann, J., Narang, K., Loh, A., Paff, M., Horn, A., Kucharczyk, W., Deeb, W., Salvato, B., Almeida, L., Foote, K.D., Rosenberg, P.B., Tang-Wai, D.F., Anderson, W.S., Mari, Z., Ponce, F.A., Wolk, D.A., Burke, A.D., Salloway, S., Sabbagh, M.N., Chakravarty, M.M., Smith, G.S., Lyketsos, C.G., Okun, M.S., Lozano, A.M., 2021. Mapping autonomic, mood, and cognitive effects of hypothalamic region deep brain stimulation. Brain doi:10.1093/brain/awab170.

Neudorfer, C., Germann, J., Elias, G.J.B., Gramer, R., Boutet, A., Lozano, A.M., 2020. A high-resolution in vivo magnetic resonance imaging atlas of the human hypothalamic region. Sci. Data 7, 305. doi:10.1038/s41597-020-00644-6.

Neudorfer, C., Kroneberg, D., Al-Fatly, B., Goede, L., Kübler, D., Faust, K., Rienen, U., Tietze, A., Picht, T., Herrington, T.M., Middlebrooks, E.H., Kühn, A., Schneider, G., Horn, A., 2022. Personalizing deep brain stimulation using advanced imaging sequences. Ann. Neurol. 00, 1–16. doi:10.1002/ana.26326.

Neumann, W.J., Schroll, H., De Almeida Marcelino, A.L., Horn, A., Ewert, S., Irmen, F., Krause, P., Schneider, G.H., Hamker, F., Kühn, A.A., 2018. Functional segregation of basal ganglia pathways in Parkinson's disease. Brain 141, 2655–2669. doi:10.1093/brain/awy206.

Niso, G., Gorgolewski, K.J., Bock, E., Brooks, T.L., Flandin, G., Gramfort, A., Henson, R.N., Jas, M., Litvak, V., Moreau, T., J, Oostenveld, R., Schoffelen, J.-.M., Tadel, F., Wexler, J., Baillet, S., 2018. MEG-BIDS, the brain imaging data structure extended to magnetoencephalography. Sci. Data 5, 180110. doi:10.1038/sdata.2018.110.

Nowacki, A., Barlatey, S., Al-Fatly, B., Dembek, T., Bot, M., Green, A.L., Kübler, D., Lachenmayer, M.L., Debove, I., Segura-Amil, A., Horn, A., Visser-Vandewalle, V., Schuurman, R., Barbe, M., Aziz, T.Z., Kühn, A.A., Nguyen, T.A.K., Pollo, C., 2022. Probabilistic mapping reveals optimal stimulation site in essential tremor. Ann. Neurol. doi:10.1002/ana.26324.

Nowacki, A., Nguyen, T.A.-K., Tinkhauser, G., Petermann, K., Debove, I., Wiest, R., Pollo, C., 2018. Accuracy of different three-dimensional subcortical human brain atlases for DBS –lead localisation. NeuroImage: Clinical 20, 868–874. doi:10.1016/j.nicl.2018.09.030.

Nowacki, A., Schober, M., Nader, L., Saryyeva, A., Nguyen, T.K., Green, A.L., Pollo, C., Krauss, J.K., Fontaine, D., Aziz, T.Z., 2020. Deep brain stimulation for chronic cluster headache: meta-analysis of individual patient data. Ann. Neurol. 88, 956–969. doi:10.1002/ana.25887.

Oxenford, S., Roediger, J., Neudorfer, C., Milosevic, L., Güttler, C., Spindler, P., Vajkoczy, P., Neumann, W.-.J., Kühn, A., Horn, A., 2021. Lead-OR: a Multimodal Platform for Deep Brain Stimulation Surgery. medRxiv 2021.08.09.21261792 doi:10.1101/2021.08.09.21261792.

Pernet, C.R., Appelhoff, S., Gorgolewski, K.J., Flandin, G., Phillips, C., Delorme, A., Oostenveld, R., 2019. EEG-BIDS, an extension to the brain imaging data structure for electroencephalography. Sci. Data 6, 103. doi:10.1038/s41597-019-0104-8.

Rappel, P., Grosberg, S., Arkadir, D., Linetsky, E., Abu Snineh, M., Bick, A.S., Tamir, I., Valsky, D., Marmor, O., Abo Foul, Y., Peled, O., Gilad, M., Daudi, C., Ben-Naim, S., Bergman, H., Israel, Z., Eitan, R., 2020. Theta-alpha oscillations characterize emotional subregion in the human ventral subthalamic nucleus. Mov. Disord. 35, 337–343. doi:10.1002/mds.27910.

Reich, M.M., Horn, A., Lange, F., Roothans, J., Paschen, S., Runge, J., Wodarg, F., Pozzi, N.G., Witt, K., Nickl, R.C., Soussand, L., Ewert, S., Maltese, V., Wittstock, M., Schneider, G.-.H., Coenen, V., Mahlknecht, P., Poewe, W., Eisner, W., Helmers, A.-.K., Matthies, C., Sturm, V., Isaias, I.U., Krauss, J.K., Kühn, A.A., Deuschl, G., Volkmann, J., 2019. Probabilistic mapping of the antidystonic effect of pallidal neurostimulation: a multicentre imaging study. Brain 142, 1386–1398. doi:10.1093/brain/awz046.

Reich, M.M., Hsu, J., Ferguson, M., Schaper, F.L.W.V.J., Joutsa, J., Roothans, J., Nickl, R.C., Frankemolle-Gilbert, A., Alberts, J., Volkmann, J., Fox, M.D., 2022. A brain network for deep brain stimulation induced cognitive decline in Parkinson's disease. Brain doi:10.1093/brain/awac012.

Sharp, G., Li, R., Wolfgang, J., Chen, G., Peroni, M., Spadea, M., Mori, S., Zhang, J., Shackleford, J., Kandasamy, N., 2010. Plastimatch—an open-source software for radiotherapy imaging. In: Proceedings of the XVI'th International Conference on the Use of Computers in Radiotherapy (ICCR). Elsevier, Amsterdam, Netherlands doi:10.1016/B978-0-12-407741-6.00006-2.

Shen, L., Jiang, C., Hubbard, C.S., Ren, J., He, C., Wang, D., Dahmani, L., Guo, Y., Liu, Y., Xu, S., Meng, F., Zhang, J., Liu, H., Li, L., 2020. Subthalamic nucleus deep brain stimulation modulates 2 distinct neurocircuits. Ann. Neurol. 88, 1178–1193. doi:10.1002/ana.25906.

Siddiqi, S.H., Schaper, F., Horn, A., Hsu, J., Cash, R.F.H., Padmanabhan, J.L., Johnson, K.A., Egorova, N., Naidech, A.M., Gozzi, S., Phan, T.G., Choi, K.S., Irmen, F., Kühn, A.A., Fitzgerald, P.B., Rouhl, R.P.W., Taylor, S.F., George, M.S., Voss, J.L., Corbetta, M., Dougherty, D.D., Pascual-Leone, A., Grafman, J.H., Mayberg, H.S., Fox, M.D., 2021. A neuroanatomical substrate for depression derived from brain lesions and brain stimulation. Nat. Hum. Behav..

Sobesky, L., Goede, L., Odekerken, V.J.J., Wang, Q., Li, N., Neudorfer, C., Rajamani, N., Al-Fatly, B., Reich, M., Volkmann, J., de Bie, R.M.A., Kühn, A.A., Horn, A., 2021a. Subthalamic and pallidal deep brain stimulation: are we modulating the same network? Brain doi:10.1093/brain/awab258.

Trapp, N.T., Bruss, J.E., Manzel, K., Grafman, J., Tranel, D., Boes, A.D., 2022. Large-scale lesion symptom mapping of depression identifies brain regions for risk and resilience. Brain awac361. doi:10.1093/brain/awac361.

Treu, S., Strange, B., Oxenford, S., Neumann, W.-.J., Kühn, A., Li, N., Horn, A., 2020. Deep brain stimulation: imaging on a group level. Neuroimage 219, 117018. doi:10.1016/j.neuroimage.2020.117018.

Tsuboi, T., Charbel, M., Peterside, D.T., Rana, M., Elkouzi, A., Deeb, W., Ramirez-Zamora, A., Lemos Melo Lobo Jofili Lopes, J., Almeida, L., Zeilman, P.R., Eisinger, R.S., Foote, K.D., Okromelidze, L., Grewal, S.S., Okun, M.S., Middlebrooks, E.H., 2021. Pallidal connectivity profiling of stimulation-induced dyskinesia in Parkinson's disease. Mov. Disord. 36, 380–388. doi:10.1002/mds.28324.

Tustison, N.J., Avants, B.B., Cook, P.A., Zheng, Yuanjie, Egan, A., Yushkevich, P.A., Gee, J.C., 2010. N4ITK: improved N3 bias correction. IEEE Trans. Med. Imaging 29, 1310–1320. doi:10.1109/TMI.2010.2046908.

Vasques, X., Cif, L., Hess, O., Gavarini, S., Mennessier, G., Coubes, P., 2009. Stereotactic model of the electrical distribution within the internal globus pallidus during deep brain stimulation. J. Comput. Neurosci. 26, 109–118. doi:10.1007/s10827-008-0101-y.

Vogel, D., Shah, A., Coste, J., Lemaire, J.J., Wårdell, K., Hemm, S., 2020. Anatomical brain structures normalization for deep brain stimulation in movement disorders. NeuroImage: Clinical 27, 102271. doi:10.1016/j.nicl.2020.102271.

Vorwerk, J., Oostenveld, R., Piastra, M.C., Magyari, L., Wolters, C.H., 2018. The FieldTrip-SimBio pipeline for EEG forward solutions. Biomed. Eng. Online 17, 37. doi:10.1186/s12938-018-0463-y.

Wang, Q., Akram, H., Muthuraman, M., Gonzalez-Escamilla, G., Sheth, S.A., Oxenford, S., Yeh, F.-.C., Groppa, S., Vanegas-Arroyave, N., Zrinzo, L., Li, N., Kühn, A., Horn, A., 2021. Normative vs. patient-specific brain connectivity in deep brain stimulation. Neuroimage 224, 117307. doi:10.1016/j.neuroimage.2020.117307.

Weigand, A., Horn, A., Caballero, R., Cooke, D., Stern, A.P., Taylor, S.F., Press, D., Pascual-Leone, A., Fox, M.D., 2018. Prospective validation that subgenual connectivity predicts antidepressant efficacy of transcranial magnetic stimulation sites. Biol. Psychiatry 84, 28–37. doi:10.1016/j.biopsych.2017.10.028.

Yeo, B.T., Krienen, F.M., Sepulcre, J., Sabuncu, M.R., Lashkari, D., Hollinshead, M., Roffman, J.L., Smoller, J.W., Zöllei, L., Polimeni, J.R., Fisch, B., Liu, H., Buckner, R.L., 2011. The organization of the human cerebral cortex estimated by intrinsic functional connectivity. J. Neurophysiol. 106, 1125–1165. doi:10.1152/jn.00338.2011.

Yu, B., Li, L., Guan, X., Xu, X., Liu, X., Yang, Q., Wei, H., Zuo, C., Zhang, Y., 2021. HybraPD atlas: towards precise subcortical nuclei segmentation using multimodality medical images in patients with Parkinson disease. Hum. Brain Mapp. 42, 4399–4421. doi:10.1002/hbm.25556.